Multiwavelength Study of the NGC 281 Region

Saurabh SHARMA,[1,2,3] Anil K. PANDEY,[1] Jeewan C. PANDEY,[1] Neelam CHAUHAN,[8] Katsuo OGURA,[4]
Devandra K. OJHA,[5] Jura BORRISSOVA,[2] Hiroyuki MITO,[6] Thomas VERDUGO,[2,9] and Bhuwan C. BHATT[7]

[1]*Aryabhatta Research Institute of Observational Sciences (ARIES), Manora Peak, Nainital, 263 129, India*
saurabh@aries.res.in
[2]*Departamento de Física y Astronomía, Universidad de Valparaíso, Ave. Gran Bretaña 1111, Valparaíso, Chile*
[3]*INAF-Osservatorio Astrofisico di Arcetri, Largo E. Fermi 5, 50125 Firenze, Italy*
[4]*Kokugakuin University, Higashi, Shibuya-ku, Tokyo 150-8440*
[5]*Tata Institute of Fundamental Research, Mumbai - 400 005, India*
[6]*Kiso Observatory, School of Science, The University of Tokyo, Mitake-mura, Kiso-gun, Nagano 397-0101*
[7]*CREST, Indian Institute of Astrophysics, Hosakote 562 114, India*
[8]*Institute of Astronomy, National Central University, Jhongli 32001, Taiwan*
[9]*Centro de Investigaciones de Astronomía (CIDA), Apartado Postal 264, Mérida 5101-A, Venezuela*

Abstract

We present a multiwavelength study of the NGC 281 complex, which contains the young cluster IC 1590 at the center, using deep wide-field optical $UBVI_{\rm c}$ photometry, slitless spectroscopy along with archival data sets in the near-infrared (NIR) and X-ray regions. The extent of IC 1590 is estimated to be ~ 6.5 pc. The cluster region shows a relatively small amount of differential reddening. The majority of the identified young stellar objects (YSOs) are low-mass PMS stars having age < 1–2 Myr and mass 0.5–3.5 $M_{\odot}$. The slope (Γ) of the mass function for IC 1590, in the mass range $2 < M/M_{\odot} \leq 54$, is found to be -1.11 ± 0.15. The slope of the K-band luminosity function (0.37 ± 0.07) is similar to the average value (~ 0.4) reported for young clusters. The distribution of gas and dust obtained from the IRAS, CO, and radio maps indicates clumpy structures around the central cluster. The radial distribution of the young stellar objects, their ages, $\Delta(H - K)$ NIR-excess, and the fraction of classical T Tauri stars suggest triggered star formation at the periphery of the cluster region. However, deeper optical, NIR, and MIR observations are needed to have a conclusive view of the star-formation scenario in the region. The properties of the Class 0/I and Class II sources detected by using the Spitzer mid-infrared observations indicate that a majority of the Class II sources are X-ray emitting stars, whereas X-ray emission is absent from the Class 0/I sources. The spatial distribution of Class 0/I and Class II sources reveals the presence of three sub-clusters in the NGC 281 West region.

Key words: Galaxy: open clusters and associations: individual (IC 1590) — stars: formation — stars: luminosity function, mass function — stars:pre–main–sequence

1. Introduction

H II regions have been studied quite extensively in recent years on account of their close association with star formation. There seems to be two modes of star formation associated with H II regions depending on the initial density distribution of the natal molecular cloud. One is the cluster mode, which gives birth to a rich open clusters; the other is the dispersed mode, which forms only loose clusters or aggregates of stars. Presumably, the former takes place in centrally condensed, massive clouds, whereas the latter occurs in clumpy, dispersed clouds (see e.g., Ogura 2006). These clusters/aggregates of stars emerging from their natal clouds can be laboratories to address some of the fundamental questions of star formation. Trends in their evolutionary states and spatial distribution can help distinguish between various star formation scenarios, such as spontaneous or triggered star formation. Triggered star formation is a complex process, which makes an interesting and important topic of concerning star formation. The formation of massive stars feeds energy back into the nearby environments, irradiating, heating, and compressing the remains of the natal molecular cloud. This feedback can have either destructive or constructive effects, but it is not clear which dominates in a given cloud, or overall in a galaxy. Many examples exist in our Galaxy as well as in other galaxies where the spatial distributions of young stellar objects (YSOs) and their ages suggest triggered star-formation (see e.g., Walborn et al. 2002; Oye et al. 2005; Deharveng et al. 2005; Sharma et al. 2007; Chauhan et al. 2009).

The H II region NGC 281/Sh 2-184 ($\alpha_{2000} = 00^{\rm h}52^{\rm m}$, $\delta_{2000} = +56°34'$ and $l = 123°07$, $b = -6°31$) is located at a relatively high galactic latitude, and has a centrally located cluster, IC 1590 (Guetter & Turner 1997; Henning et al. 1994). The brightest member of IC 1590 is an O-type Trapezium-like system, HD 5005, whose component stars, HD 5005ab (unresolved), HD 5005c, and HD 5005d, have spectral types of O6.5 V, O8 V, and O9 V, respectively (Walborn 1973; Abt 1986; Guetter & Turner 1997). Despite many measurements, the distance estimate of NGC 281 varies from 2.0 kpc to 3.7 kpc (cf. Sato et al. 2008). Recently, using VLBI observations of an associated H_2O maser source, Sato et al. (2008) derived a trigonometric parallax of 0.355 ± 0.030 milliarcsec,

corresponding to a distance of $2.81 \pm 0.24\,\mathrm{kpc}$.

The NGC 281 region provides an excellent laboratory for studying in detail star formation through the interaction of high-mass stars with their surrounding cloud. Of special interest in this region is the possibility of triggered star formation occurring on two different scales: large-scale ($\sim 300\,\mathrm{pc}$) supernova-triggered formation of the first generation OB stars and their associated cluster (Megeath et al. 2002, 2003), and subsequent, triggered sequential, and ongoing star formation on a smaller scale (~ 1–$10\,\mathrm{pc}$); the latter is taking place in an adjoining molecular cloud (NGC 281 West), probably through an interaction with an H II region (the NGC 281 nebula) excited by the first-generation OB stars (Elmegreen & Lada 1978; Megeath & Wilson 1997; Sato et al. 2008).

The southwestern quadrant of the NGC 281 nebula is obscured by an adjoining molecular cloud, NGC 281 West. Ongoing star formation in NGC 281 West is indicated by the presence of H_2O maser emission and IRAS sources within this cloud near its clumpy interface between the H II region. This star formation may have been triggered by the interaction of the molecular cloud with the H II region (Elmegreen & Lada 1978; Megeath & Wilson 1997). The NGC 281 molecular cloud complex was mapped both in $^{12}\mathrm{CO}$ ($J = 1$–0) and $^{13}\mathrm{CO}$ ($J = 1$–0) emission lines by Lee and Jung (2003). The central radial velocity of the NGC 281 West molecular cloud, $V_{\mathrm{LSR}} = 31\,\mathrm{km\,s^{-1}}$ (Lee & Jung 2003), agrees well with that of the H_2O maser emission in the cloud (Sato et al. 2007). Megeath et al. (2002, 2003) suggested that this cloud complex was formed in a fragmenting super-bubble, which gave birth to the first-generation OB stars, and these OB stars then ionised the surrounding gas, which subsequently triggered next-generation star formation in the neighboring clouds (Sato et al. 2008).

Though both low-mass and high-mass star-forming regions can be studied at variety of wavelengths, ranging from radio waves to X-rays, however most of the present knowledge about the H II region/open cluster NGC 281 has been inferred from studies outside the optical region. Henning et al. (1994) made multiwavelength studies of the NGC 281/IC 1590 region, including Strömgren photometry of the bright cluster stars. The first detailed UBV CCD photometry of 279 stars for the cluster was published by Guetter and Turner (1997). Their photometry terminates at a magnitude limit that is marginally brighter than the expected brightness of pre-main sequence (PMS) and T Tauri stars in the embedded cluster region. Keeping the above discussion in mind, we feel that NGC 281 is an appropriate target for a deep and wide field optical/infrared photometry. In this paper, we present deep wide-field optical $UBVI_{\mathrm{c}}$ data and slitless spectroscopy. We supplement them with archival data collected from surveys, such as Chandra, Spitzer, 2MASS, IRAS, and NVSS (NRAO VLA Sky Survey). Our aim is to understand the global scenario of star formation under the effects of massive stars in the whole NGC 281/IC 1590 region. In section 2, we describe our optical CCD photometric and slitless spectroscopic observations, and briefly the data reduction. In section 3, we discuss the archival data set used in the present study. In the ensuing sections, we present the results and discuss star-formation scenarios in the NGC 281 region.

Table 1. Log of observations.

Date of observation/Filter	Exp(s) × frames
Kiso Schmidt telescope, Japan	
2004 November 21	
B	$60 \times 6, 20 \times 6$
V	$60 \times 6, 10 \times 6$
I_{c}	$60 \times 6, 10 \times 6$
2005 November 27	
U	$180 \times 6, 60 \times 2$
I_{c}	10×2
Sampurnanand telescope, ARIES	
2005 January 07	
U	$300 \times 3, 120 \times 1, 30 \times 1$
B	$120 \times 3, 30 \times 3$
V	$120 \times 3, 30 \times 3$
I_{c}	$60 \times 4, 10 \times 3$
Himalayan Chandra Telescope, IIA	
2005 October 10	
Slitless spectra	$(420 \times 3) \times 4$
Direct frames	$(60 \times 3) \times 4$
2006 August 16	
Slitless spectra	$(300 \times 2) \times 4$
Direct frames	$(60 \times 1) \times 4$

2. Observations and Data Reduction

2.1. Optical Photometry

The CCD $UBVI_{\mathrm{c}}$ observations of the NGC 281 region were obtained by using the 105-cm Schmidt telescope of the Kiso Observatory, Japan on 2004 November 21 and 2005 November 27. The CCD camera used a SITe 2048 pixel $\times$ 2048 pixel TK2048E chip having a pixel size of $24\,\mu\mathrm{m}$. At the Schmidt focus ($f/3.1$), each pixel corresponds to $1{.}''5$, and the entire chip covers a field of $\sim 50' \times 50'$ on the sky. The read-out noise and gain of the CCD are $23.2\,e^-$ and $3.4\,e^-/\mathrm{ADU}$, respectively. A number of short and deep exposure frames were taken. The average FWHM of star images was found to be $\sim 3''$. The observed region is shown in figure 1. The Kiso data were standardized by observing the cluster together with the standard stars in the SA 98 field (Landolt 1992) on 2005 January 07 using the 2048 pixel $\times$ 2048 pixel CCD camera mounted on the $f/13$ Cassegrain focus of the 104-cm Sampurnanand telescope of Aryabhatta Research Institute of Observational Sciences (ARIES), Nainital. In this set up, each pixel of the CCD corresponds to $\sim 0{.}''37$, and the entire chip covers a field of $\sim 13' \times 13'$ on the sky. To improve the signal-to-noise ratio, this observation was carried out in a binning mode of 2×2 pixel. The read-out noise and gain of the CCD are $5.3\,e^-$ and $10\,e^-/\mathrm{ADU}$, respectively. The FWHMs of the star images were $\sim 2''$. The log of these observations is given in table 1.

The CCD data frames were reduced by using computing facilities available at ARIES, Nainital. Initial processing of the data frames was done using the standard tasks available from IRAF[1] and ESO-MIDAS[2] data-reduction packages. Photometry of cleaned frames was carried out by using
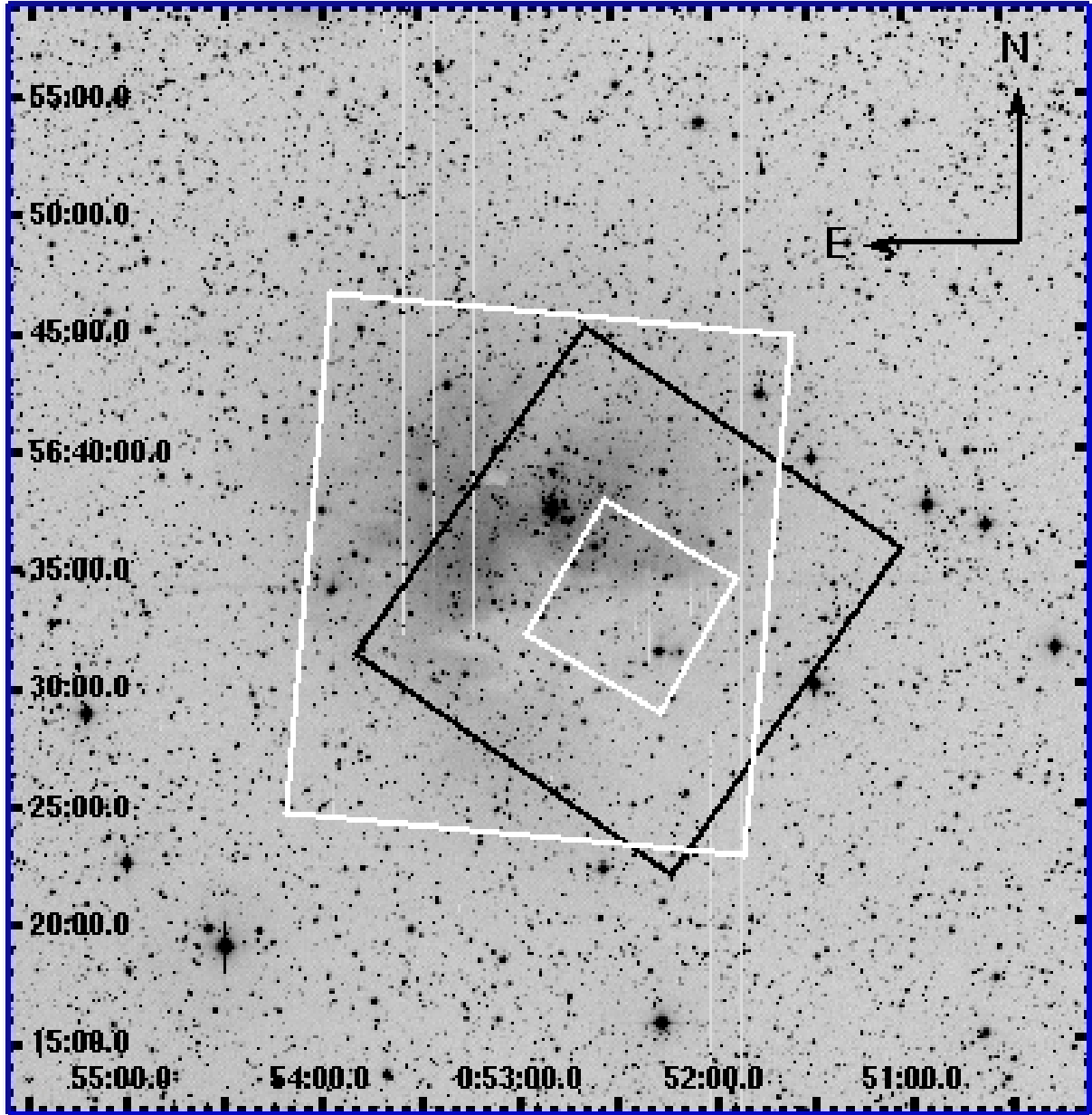
Fig. 1. *V* band image of the NGC 281 region taken with the Kiso Schmidt. The big and small white boxes are areas covered by the Hα and Spitzer observations, the black box represents the Chandra observations. The *X* and *Y* axes are in *RA* and *Dec* in J2000.

the DAOPHOT-II software (Stetson 1987). The PSF was obtained for each frame by using several uncontaminated stars. Magnitudes obtained from different frames were averaged. When brighter stars were saturated on deep exposure frames, their magnitudes were taken from short exposure frames. We used the DAOGROW program for constructing an aperture growth curve required for determining the difference between the aperture and profile fitting magnitudes. Calibration of the instrumental magnitudes to those in the standard system was done by using procedures outlined by Stetson (1992).

To translate the instrumental magnitudes to the standard

magnitudes, the following calibration equations, derived using a least-squares linear regression, were used:

$$u = U + (7.004 \pm 0.004) - (0.005 \pm 0.006)(U - B)$$
$$+ (0.431 \pm 0.005)X, \tag{1}$$
$$b = B + (4.742 \pm 0.005) - (0.035 \pm 0.004)(B - V)$$
$$+ (0.219 \pm 0.004)X, \tag{2}$$
$$v = V + (4.298 \pm 0.002) - (0.038 \pm 0.002)(V - I)$$
$$+ (0.128 \pm 0.002)X, \tag{3}$$
$$i = I_c + (4.701 \pm 0.004) - (0.059 \pm 0.003)(V - I)$$
$$+ (0.044 \pm 0.003)X \tag{4}$$

where U, B, V, and I_c are the standard magnitudes and u, b, v, and i are the instrumental aperture magnitudes normalized

---

[1] IRAF is distributed by National Optical Astronomy Observatories, USA.

[2] ESO-MIDAS is developed and maintained by the European Southern Observatory.

Table 2. Completeness Factor (CF) of the optical photometric data in the cluster and field regions.

V range (mag)	IC 1590 $r \leq 2'$	$2' < r \leq 5'$	Field region $r > 5'$
9.5–10.5	1.00	1.00	1.00
10.5–11.5	1.00	1.00	1.00
11.5–12.5	1.00	1.00	1.00
12.5–13.5	1.00	1.00	1.00
13.5–14.5	1.00	1.00	1.00
14.5–15.5	1.00	0.96	0.98
15.5–16.5	0.93	0.97	0.95
16.5–17.5	0.74	0.94	0.96
17.5–18.5	0.62	0.90	0.90
18.5–19.5	0.32	0.40	0.45

for 1 second of exposure time and X is the airmass. We have ignored the second-order colour correction terms, since they are generally small in comparison to other errors present in the photometric data reduction. The standard deviations of the standardization residuals, Δ, between the standard and transformed V magnitude and $(U - B)$, $(B - V)$, and $(V - I)$ colours of the standard stars are 0.006, 0.025, 0.015, and 0.015 mag, respectively. Short exposure data of the cluster region, taken on the standardization nights, were standardized by using the above equations and coefficients. The standard magnitudes and colours of more than 50 stars obtained from these short exposures were further used to standardize the deep observations taken with Kiso Schmidt. The standard deviations of the residual of secondary standards are on the order ~ 0.02 mag. The typical DAOPHOT errors in magnitude as a function of the corresponding magnitude in different passbands for the Kiso Schmidt observations are found to increase with the magnitude, and become large (≥ 0.1 mag) for stars fainter than $V \simeq 20$ mag. Measurements beyond this magnitude were not considered in the analysis.

2.1.1. Completeness of the data

To study luminosity functions (LFs)/mass functions (MFs), it is very important to make necessary corrections in any data sample to take into account the incompleteness that may occur for various reasons (e.g., crowding of the stars). We used the ADDSTAR routine of DAOPHOT II to determine the completeness factor (CF). The procedures were outlined in detail in our earlier works (Pandey et al. 2001, 2005). Briefly, the method consists of randomly adding artificial stars of known magnitude and position into the original frame. The frames are re-reduced using the same procedure as used for the original frame. The ratio of the number of stars recovered to those added in each magnitude interval gives the CF as a function of magnitude. In the case of optical CCD photometry, the incompleteness of the data increases with the magnitude, as expected. The CF as a function of the V magnitude is given in table 2. Table 2 indicates that our optical data have a 95% completeness at $V \sim 16.5$ mag, which corresponds to a stellar mass of $\sim 2\,M_\odot$ for a PMS star having an age of ~ 2 Myr (cf. figure 11).

2.1.2. Comparison with previous studies

We carried out a comparison of the present photometric data with those available in the literature. The difference, Δ(literature − present data), as a function of the V magnitude is given in table 3. The comparison indicates that the present V mag and $(B - V)$ colours are in good agreement with the CCD and photoelectric photometry by Guetter and Turner (1997), whereas $\Delta(U - B)$ shows a systematic variation with the V magnitude in the sense that the present $(U - B)$ colours become blue with increasing V magnitude.

2.2. Slitless Grism Spectroscopy

The spectra of some PMS stars, specifically classical T Tauri stars (CTTSs), show emission lines, among which usually Hα is the strongest. Therefore, Hα surveys have often been used to identify PMS stars. We observed the NGC 281 region in the slitless mode with a grism as the dispersing element using the Himalayan Faint Object Spectrograph Camera (HFOSC) instrument during two observing runs on 2005 October 10 and 2006 August 16. This yielded panoramic images where the star images are replaced by their spectra. The combination of a 'wide Hα' interference filter (6300–6740 Å) and Grism 5 (resolution = 870) of HFOSC was used without any slit. The central $2\,K \times 2\,K$ pixels of the $2\,K \times 4\,K$ CCD were used in the observations. The pixel size was $15\,\mu$m with an image scale of $0''.297$ pixel^{-1}. The observed sky area is shown in figure 1 as a large white box, which was covered by four field-of-views of $\sim 10 \times 10$, each. For each field-of-view we secured three spectroscopic frames of longer exposure with the grism in, and one direct frame of shorter exposure with the grism out for the purpose of identification. The log of the observations is given in table 1. Emission-line stars with enhancement over the continuum at the Hα wavelength are visually identified.

3. Archival Datasets

3.1. 2MASS

Near-infrared (NIR) JHK_s data for point sources in the NGC 281 region have been obtained from the Two Micron All Sky Survey (2MASS) Point Source Catalogue. The 2MASS data was reported to be 99% complete up to ~ 16, 15, 14.7 mag in the J, H, K_s bands respectively.[3] To secure photometric accuracy, we used only photometric data with the quality flag ph-qual=AAA, which endorses an $S/N \geq 10$ and a photometric uncertainty < 0.10 mag. The NIR data were used to identify the Classical T Tauri stars (CTTSs) and Weak line T Tauri stars (WTTSs) (cf. subsection 4.3).

3.2. Chandra X-Ray Data

Since YSOs are very strong X-ray emitters (as strong as $\log L_X/L_{bol} \sim 10^{-3}$), and they can be detected behind column densities as large as $N_{HI} \sim 10^{23}$ cm^2 (Linsky et al. 2007), X-ray imaging of star-forming regions and young clusters is valuable for identifying these sources.

3.2.1. Observation

Chandra observed the NGC 281 region on three occasions for 62.6 ks (Obs ID 5424, on 2005-11-10 @ 18:19:27 UT),

---

[3] See ⟨http://www.ipac.caltech.edu/2mass/releases/allsky/doc/sec6_5a1.html⟩.

Table 3. Comparison of the present photometry with the available photometry in the literature.[*]

V range	$\Delta(V)$ (Mean $\pm\,\sigma$)	(N)	$\Delta(B-V)$ (Mean $\pm\,\sigma$)	(N)	$\Delta(U-B)$ (Mean $\pm\,\sigma$)	(N)
Guetter and Turner (1997, ccd)						
< 12	-0.004 ± 0.019	5	-0.022 ± 0.016	5	-0.046 ± 0.046	5
12–13	0.001 ± 0.031	5	-0.019 ± 0.010	5	-0.038 ± 0.049	5
13–14	-0.011 ± 0.022	18	0.002 ± 0.018	18	-0.040 ± 0.075	16
14–15	0.022 ± 0.042	16	-0.014 ± 0.022	16	0.010 ± 0.086	14
15–16	0.011 ± 0.040	40	0.011 ± 0.035	40	0.051 ± 0.102	21
16–17	0.021 ± 0.053	52	-0.026 ± 0.042	50	—	—
17–18	0.036 ± 0.062	16	-0.002 ± 0.077	16	—	—
Guetter and Turner (1997, pe)						
< 12	-0.001 ± 0.014	5	-0.030 ± 0.013	5	-0.054 ± 0.038	5
12–13	-0.018 ± 0.011	4	-0.016 ± 0.014	4	-0.059 ± 0.040	4
13–14	0.015 ± 0.011	4	-0.013 ± 0.014	4	-0.083 ± 0.045	4

[*] The difference Δ(literature $-$ present data) is in magnitude. Mean and σ are based on N stars in a V magnitude bin. ccd: charged coupled device data. pe: photo-electric data.

23.5 ks (Obs ID 7206, 2005-11-08 @ 13:41:46 UT) and 13.1 ks (Obs ID 7205 @ 22:40:54 UT). The aim point of the array was $\alpha_{2000} = 00^{\mathrm{h}}52^{\mathrm{m}}25\overset{\mathrm{s}}{.}2$, $\delta_{2000} = +56°33'47''.6$, and the satellite roll angle (i.e., the orientation of the CCD array relative to the north–south direction) was $225°.5$ for all observations. The exposures were obtained in the very faint data mode with a 3.2 s frame time using the ACIS-I imaging array as the primary detector. ACIS-I consists of four front illuminated 1024×1024 CCDs with a pixel size of $\sim 0''.492$ and a combined field of view of $\approx 16'.9 \times 16'.9$. Although the S2 and S3 CCDs in ACIS-S were also enabled, in the present study we used any the ACIS-I data. Detailed information on Chandra and its instrumentation can be found in the Chandra Proposer's Guide (POG).[4] To detect sources, we merged the event-list files of all observations. The X-ray observed region is again shown in figure 1 by a black box.

3.2.2. Data reduction and source detection

We analyzed the data reprocessed by the Chandra X-Ray Center on 2006 April 5 (ASCDSVER 7.6.7.1). The data were reduced by using the Chandra Interactive Analysis of Observations (CIAO: Fruscione et al. 2006) software (ver. 4.1; CALDB ver. 4.2). Light curves from the on-chip background regions were inspected for large background fluctuations that might have resulted from solar flares; none were found. We filtered the data for the energy band 0.5 to 7.5 keV. After filtering in energy, the time-integrated background was 0.11 counts arcsec^{-2}. Source detection was performed on the merge-event list by using a 1.7 keV exposure map with the PWDetect[5] code (Damiani et al. 1997), a wavelet-based source detection algorithm. The significance threshold was set to $5\,\sigma$ so as to ensure a maximum of one spurious source per field. We detected 379 sources, out of which 9 sources either fell on the unexposed areas of the CCD or were doubly detected. This implies that a total of 370 X-ray sources were detected in the NGC 281 field. An IDL-based program ACIS Extract (AE:

Broos et al 2010) was used to extract the photons from each candidate source in a polygonal region that closely matched with the local PSFs. The source-free regions around the source were considered as background. AE provides the Poisson probability of not being a source. We did not consider those sources that had a probability of being non-existence > 0.01. Sixteen such sources were found in the catalogue. After removing these sources, the catalogue consisted of 354 X-ray sources. Further, the median-detected photon energy for the point sources were determined by using the ACIS Extract software package. We estimated the background AGN rate within the Chandra field of view using the Chandra Deep Field (Brandt et al. 2001). At the 0.5–2 keV limiting flux of 5.6×10^{-16} erg s^{-1} cm^{-2}, we expected to find 79 to 127 background objects within the Chandra field of view. The optical, 2MASS, and IRAC (Infrared Array Camera) counterparts of the X-ray sources were searched within a match radius of $1''$, and the data are given in table 4. A sample of the table is given here, whereas the complete table is available in the electronic form only. Out of 354 X-ray sources, 193 and 90 sources have NIR and optical counterparts, respectively. All of the optical counterparts of X-ray also sources have NIR counterparts. The location of X-ray sources in the NIR colour–colour diagram has been used to identify the probable WTTSs/Class III sources. The completeness of the X-ray data has not been estimated. Since we are using the WTTSs/Class III sources to study the spatial distribution of these sources, and to support the results obtained on the basis of rather complete optical and NIR data, the incompleteness of the X-ray data will not have any significant effect on the results presented in this study.

3.3. Spitzer IRAC Data

The Spitzer mid-infrared (MIR) surveys have enabled a detailed census of YSOs in star-forming regions. The classification of young stars as protostellar Class I or more evolved Class II sources with optically thick discs is best accomplished by using their broadband spectral energy distributions (SEDs) (Muench et al. 2007).

---

[4] See ⟨http://asc.harvard.edu/proposer/POG⟩.
[5] See ⟨http://www.astropa.unipa.it/progetti_ricerca/PWDetect/⟩.

Table 4. Optical, 2MASS, and IRAC counterparts of X-ray sources searched within a match radius of $1''$.*

Radial distance (')	α_{2000} ($^{h}:^{m}:^{s}$)	δ_{2000} ($^{\circ}:':''$)	V (mag)	$(V-I)$ (mag)	J (mag)	H (mag)	K_{s} (mag)	3.6 μm (mag)	4.5 μm (mag)
0.07	00:52:39.23	+56:37:49.1	16.095	1.381	13.711	13.035	12.943	—	—
0.17	00:52:38.84	+56:37:37.0	14.391	1.029	12.707	12.229	12.115	—	—
0.41	00:52:38.64	+56:38:09.2	19.155	1.837	16.015	15.501	15.047	—	—
0.44	00:52:42.48	+56:37:55.9	—	—	16.060	15.143	15.056	—	—
0.54	00:52:35.82	+56:37:33.6	17.766	1.674	14.829	13.875	13.289	—	—
—	—	—	—	—	—	—	—	—	—
—	—	—	—	—	—	—	—	—	—
—	—	—	—	—	—	—	—	—	—

* The radial distance is from the cluster center. The complete table is available in the electronic form only ⟨http://pasj.asj.or.jp/v64/n5/640107/⟩.

Table 5. 2MASS, optical, and X-ray counterparts of IRAC sources searched within a match radius of $1''$.*

Radial distance (')	α_{2000} ($^{h}:^{m}:^{s}$)	δ_{2000} ($^{\circ}:':''$)	3.6 μm (mag)	4.5 μm (mag)	J (mag)	H (mag)	K_{s} (mag)	V (mag)	$(V-I)$ (mag)	X-rays (Y/N)
0.95	00:52:33.90	+56:37:11.8	13.821	13.391	15.937	14.981	14.606	19.876	2.169	N
1.00	00:52:34.16	+56:37:04.2	12.265	12.171	13.391	12.628	12.366	16.323	1.636	N
1.24	00:52:31.18	+56:37:16.5	15.283	15.177	16.090	15.485	15.266	—	—	N
1.24	00:52:34.00	+56:36:46.3	14.390	14.426	15.233	14.619	14.460	17.617	1.409	N
1.25	00:52:31.32	+56:37:12.1	14.461	14.463	15.208	14.566	14.494	17.169	1.217	N
—	—	—	—	—	—	—	—	—	—	—
—	—	—	—	—	—	—	—	—	—	—
—	—	—	—	—	—	—	—	—	—	—

* The radial distance is from the cluster center. The complete table is available in the electronic form only ⟨http://pasj.asj.or.jp/v64/n5/640107/⟩.

Table 6. Details of the identified cold IRAS point source.

IRAS PSC	α_{2000} ($^{h}:^{m}:^{s}$)	δ_{2000} ($^{\circ}:':''$)	F_{12} (Jy)	F_{25} (Jy)	F_{60} (Jy)	F_{100} (Jy)
00512+5617	00:54:14.74	+56:33:22.7	1.98	10.84	44.81	218.20

We have used archived MIR data observed with the IRAC. We obtained basic calibrated data (BCD) using the software Leopard. The exposure time of each BCD was 10.4 s and for each mosaic, 72 BCDs were used. Mosaicking was performed by using the MOPEX software provided by Spitzer Science Center (SSC). All of our mosaics were built at a native instrument resolution of $1''.2$ pixel^{-1} with the standard BCDs. In order to avoid source confusion due to crowding, PSF photometry for all of the sources was carried out. We used the DAOPHOT package available with the IRAF photometry routine to detect sources and to perform photometry in each IRAC band. The FWHM of every detection was measured, and all detections with an FWHM $> 3''.6$ were considered to be resolved and removed. The detections were also examined visually in each band to remove non-stellar objects and false detections. The sources with photometric uncertainties < 0.2 mag in each band were considered to be good detections. A total of 347 sources were detected in the 3.6 and 4.5 μm bands, whereas only 35 sources could be detected in all four bands.

Aperture photometry for well-isolated sources was done by using an aperture radius of $3''.6$ with a concentric sky annulus of the inner and outer radii of $3''.6$ and $8''.4$, respectively. We adopted the zero-point magnitudes for the standard aperture radius ($12''$) and background annulus of ($12''$–$22''.4$) of 19.670, 18.921, 16.855, and 17.394 in the 3.6, 4.5, 5.8, and 8.0 μm bands, respectively. Aperture corrections were also made by using the values described in the IRAC Data Handbook.[6] The necessary aperture correction for the PSF photometry was then calculated from the selected isolated sources, and were applied to the PSF magnitudes of all the sources. The 2MASS, optical, and X-ray counterparts of the IRAC sources were searched for within a match radius of $1''$. These counterparts are given in table 5. A sample of the table is given here, whereas the entire table is available in the electronic form. The completeness of the data in the 3.6, 4.5, 5.8, and 8.0 μm bands having $S/N > 5$ (error ≤ 0.2 mag) is found to be ~ 16.0, 15.5, 13.0, and 12.0 mag, respectively.

---

[6] W. Reach et al. 2006, Infrared Array Camera Data Handbook, version 3.0.
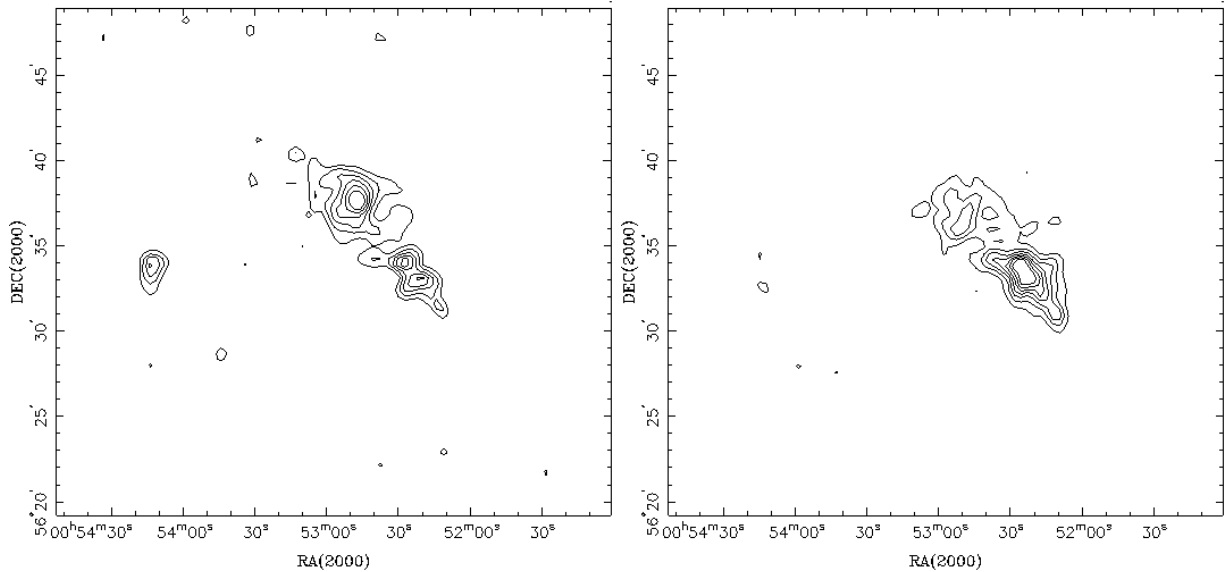
Fig. 2. (left panel) Isodensity contours of the distribution of the 2MASS sources. The contours are plotted above 3σ levels with a step size of 5 stars/pc^2. The lowest contour represents 17 stars/pc^2. (right panel) Isodensity contours of the distribution of the identified YSOs.

3.4. IRAS

The data from the IRAS survey in the four bands (12, 25, 60, and 100 μm) for the NGC 281 region were used to study the spatial distribution of warm and cold interstellar dust. One cold IRAS point source was identified in the cluster region; and its details are given in table 6.

4. Results

4.1. Structure of the Cluster

4.1.1. Isodensity contours

An internal interaction due to two-body encounters among member stars and external tidal forces due to the galactic disc or giant molecular clouds can significantly influence the morphology of clusters. However, in the case of young clusters, where dynamical relaxation is not important because of their young age, the stellar distribution can be considered as the initial state of the cluster that should be governed by the star-formation process in the parent molecular cloud (Chen et al. 2004). To study the morphology of the NGC 281 cluster, we give a plot of the isodensity contours using the 2MASS data as well as a table of the identified YSOs (cf. subsection 4.3) in figure 2. The isodensity contours indicate an elongated morphology for the cluster. It is interesting to point out that sub-structures can be clearly seen in the 2MASS data (left panel of figure 2) towards the south-west of the cluster as well as in the south-east.

4.1.2. Radial stellar surface density profile

To determine the extent and radial stellar density profile of IC 1590 we used the 2MASS data of $K \lesssim 14.3$. First, the cluster center was determined by using the stellar density distribution in a 100 pixel wide strip along both the X and Y directions around an initially eye-estimated center. The point of maximum density obtained by fitting the Gaussian distribution
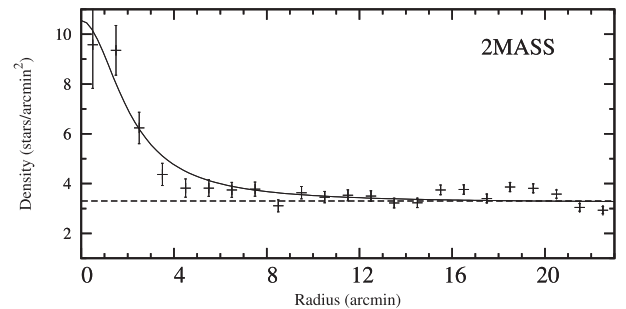

Fig. 3. Radial density profile of the cluster using the 2MASS data. The continuous curve shows a least-squares fit of the King (1962) profile to the observed data points. The error bars represent $\pm\sqrt{N}$ errors. The dashed line indicates the density of field stars.

is considered to be the center of the cluster. It is found to be $\alpha_{2000} = 00^{\rm h}52^{\rm m}39\!\!.\!^{\rm s}5 \pm 1\!\!.\!^{\rm s}0$, $\delta_{2000} = +56°37'46'' \pm 15''$.

To determine the radial surface density profile we assumed a spherical symmetry of the stellar distribution, and divided the cluster into a number of concentric circles. The projected radial stellar density in each concentric annulus was obtained by dividing the number of stars by its area. The thus-obtained densities are plotted in figure 3. The error bars were derived by assuming that the number of stars in a concentric annulus follows Poisson statistics. The horizontal dashed line in the plot indicates the density of contaminating field stars, which was obtained from the reference region $\sim 15'$ away toward the northwest from the cluster center ($\alpha_{2000} = 00^{\rm h}51^{\rm m}16\!\!.\!^{\rm s}0$, $\delta_{2000} = +56°46'45''$). The extent of the cluster, $R_{\rm cl}$, is defined as the projected radius from the density peak to the point at which the radial density becomes constant and merges with the field star density. $R_{\rm cl}$ from the optical data as well as from the NIR 2MASS data is estimated to be $\sim 8'$ (~ 6.5 pc for a distance of 2.81 kpc).
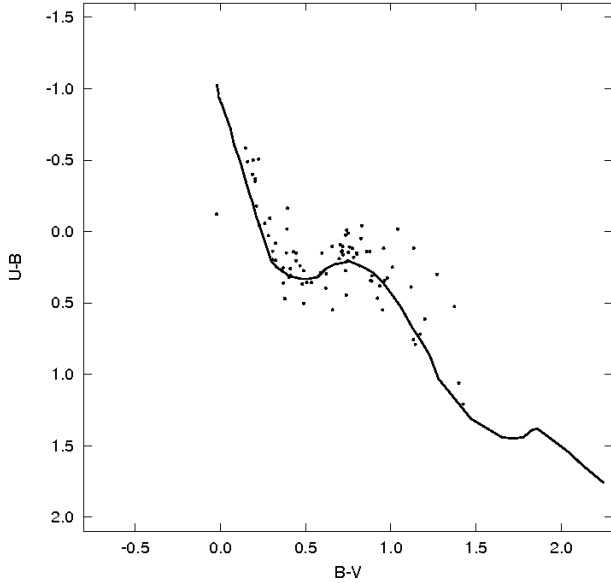
Fig. 4. $(U-B)/(B-V)$ TCD for stars lying within the cluster region ($r < 5'$). The continuous curve represents the intrinsic MS by Schmidt-Kaler (1982) shifted along the reddening vector of 0.72 for $E(B-V) = 0.32$ mag.

The observed radial density profile of the cluster was parametrized by following the approach of Kaluzny and Udalski (1992). The projected radial density profile, $\rho(r)$, is described as

$$\rho(r) = \frac{\rho_0}{1 + \left(\dfrac{r}{r_c}\right)^2},\qquad(5)$$

where the core radius, r_c, is the radial distance at which the value of $\rho(r)$ becomes half of the central density, ρ_0. The best fit obtained by the χ^2 minimization technique is shown in figure 3. Within the uncertainties the model reproduces well the observed radial density profile of IC 1590. The core radius, r_c, tunes out to be $1'.7 \pm 0'.4$ (1.4 ± 0.3 pc) and $2'.0 \pm 0'.3$ (1.6 ± 0.2 pc) for the optical and 2MASS data, respectively.

4.2. Interstellar Extinction

4.2.1. Reddening

Interstellar extinction in the cluster region was studied by using the $(U-B)/(B-V)$ two-colour diagram (TCD) shown in figure 4, where the zero-age-main-sequence (ZAMS) from Schmidt–Kaler (1982) is shifted along the normal reddening vector having a slope of $E(U-B)/E(B-V) = 0.72$. The distribution of stars shows a small amount of differential reddening [$E(B-V) \sim 0.2$ mag] in the region with a minimum of ~ 0.32 mag, which corresponds to the foreground extinction.

The reddening for individual stars having a photometric error in the V band $\sigma_V \le 0.1$ mag and of a spectral type earlier than A0 has also been estimated by using the reddening-free index, Q (Johnson & Morgan 1953). Assuming the normal reddening slope, we can construct the reddening-free index, $Q = (U-B) - 0.72 \times (B-V)$. For stars earlier than A0, the value of Q will be less than 0.0. For main-sequence (MS)

stars, the intrinsic $(B-V)_0$ colour and colour-excess can be obtained from the relation $(B-V)_0 = 0.332 \times Q$ (Johnson 1966; Hillenbrand et al. 1993) and $E(B-V) = (B-V) - (B-V)_0$, respectively. The individual reddening of stars down to the A0 spectral type is found to vary in the range of $E(B-V) \sim 0.32$–0.52 mag, implying the presence of a small amount of differential reddening.

4.2.2. Reddening law

Extinction in star clusters arises due to two distinct sources: (i) the general interstellar medium (ISM) in the foreground of the cluster, and (ii) localised dust associated with the cluster. While for the former component a value of $R = 3.1$ is well accepted (Wegner 1993; Lada & Lada 1995; Winkler 1997), for intra-cluster extinction the R value varies from 2.42 (Tapia et al. 1991) to 4.9 (Pandey et al. 2000 and references therein), or even higher, depending upon the conditions occurring in the region.

To study the nature of the extinction law in the IC 1590 region, we used TCDs as described in Pandey et al. (2000, 2003). TCDs of the form of $(V-\lambda)$ vs. $(B-V)$, where λ is one of the colour bands R, I, J, H, K, and L, provide an effective method for separating the influence of possible abnormal extinction arising within intra-cluster regions having a peculiar distribution of dust sizes from that of the normal extinction produced by the diffuse interstellar medium (cf. Chini et al. 1990; Pandey et al. 2000). The TCDs for the nearby reference region, well away from IC 1590 (see sub-subsection 4.1.2), yield the slopes of the distributions for $(V-I)$, $(V-J)$, $(V-H)$, $(V-K)$ vs. $(B-V)$ as 1.06 ± 0.03, 1.97 ± 0.05, 2.50 ± 0.06, and 2.68 ± 0.06, respectively, manifesting a normal reddening law for the foreground interstellar matter (cf. Pandey et al. 2000).

The $(V-K)$ vs. $(B-V)$ TCDs for the reference and cluster regions are shown in figure 5. Contamination due to field stars is apparent in the cluster region. We selected probable field stars having $(B-V) > 0.7$ visually, assuming that stars following the slope of the distribution of the reference region are contaminating foreground stars in the cluster region; they are shown by filled circles. The slopes of the distributions for the probable cluster members (open circles), m_{cluster}, are found to be 1.24 ± 0.04, 2.16 ± 0.06, 2.76 ± 0.08, 2.90 ± 0.09 for the $(V-I)$, $(V-J)$, $(V-H)$, $(V-K)$ vs. $(B-V)$ TCDs, respectively. The ratios $\dfrac{E(V-\lambda)}{E(B-V)}$ and the ratio of the total-to-selective extinction in the cluster region, R_{cluster}, is then derived using the procedure given by Pandey et al. (2003). R_{cluster} has turned out to be 3.5 ± 0.3. From the photometry of bright cluster members in the I and K bands and a variable-extinction analysis of ZAMS members, Guetter and Turner (1997) also found the value of R to be 3.44 ± 0.07, which is comparable to ours. Several studies have already pointed out anomalous reddening laws with high R values in the vicinity of star-forming regions (see e.g., Pandey et al. 2003 and references therein). The higher than normal values of R have been attributed to the presence of larger dust grains. There is evidence that within dark clouds the accretion of ice mantles on grains and their coagulation due to collision changes the size distribution towards larger dust particles.
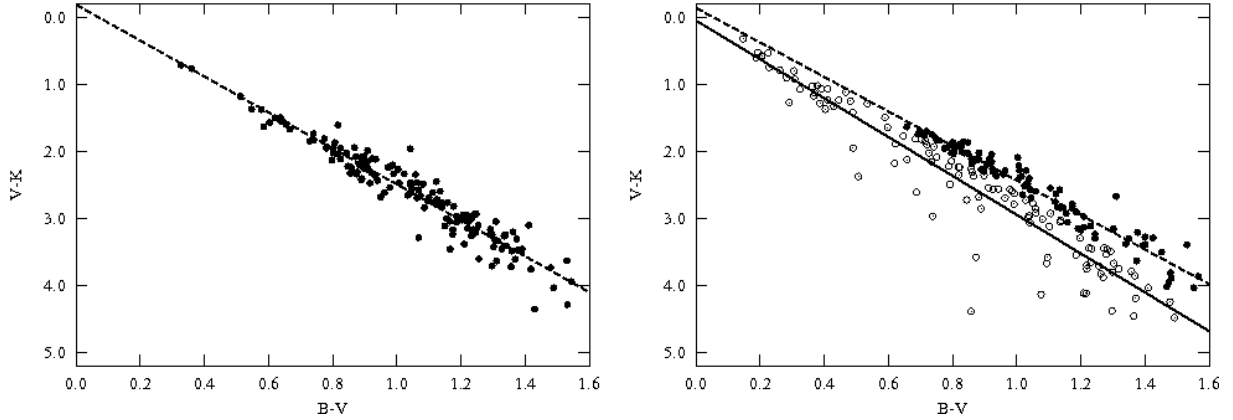
Fig. 5. $(V - K)$ vs. $(B - V)$ TCDs for the nearby reference region (left panel) and for the cluster region $(r < R_{cl})$ (right panel). Open and filled circles represent probable cluster members and field stars with normal reddening, respectively. The continuous lines show the least-squares fits to the distributions of the probable cluster members. The dashed lines show fits to distribution of field stars.
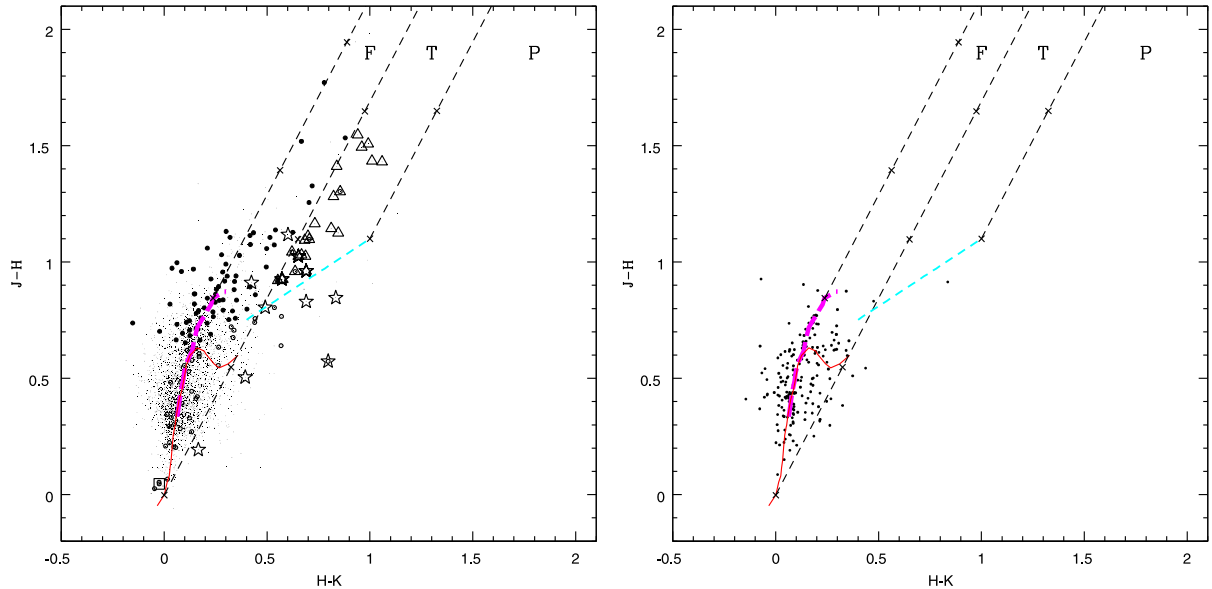

Fig. 6. (left panel) NIR TCD of the X-ray sources (open circles), Hα emission (star symbols), NIR-excess sources (open triangles), probable WTTSs (filled circles), and O-type star (open square), having photometric errors of less than 0.1 mag, in the NGC 281 region. (right panel) Same as left panel, but for all sources in the reference region detected in the JHK_s bands with photometric errors less than 0.1 mag. The sequences for dwarfs (solid curve) and giants (thick dashed curve) are taken from Bessell and Brett (1988). The dotted line represents the loci of unreddened T Tauri stars (Meyer et al. 1997). Dashed straight lines represent the reddening vectors (see the text). The crosses on the dashed lines are separated by $A_V = 5$ mag.

4.3. Identification of YSOs

4.3.1. On the basis of $(J - H)/(H - K)$ TCD

NIR imaging surveys are a powerful tool to detect YSOs in star-forming regions. The locations of YSOs on $(J - H)/(H - K)$ two-colour diagrams (NIR TCDs) are determined to a large extent by their evolutionary state. Protostellar-like objects, CTTSs, weak-line T Tauri stars (WTTSs), Herbig Ae/Be stars, and classical Be stars tend to occupy different regions on NIR TCDs.

The NIR TCD using the 2MASS data for all sources lying in the NGC 281 region and having photometric errors of less than 0.1 magnitude is shown in the left panel of figure 6. All of the 2MASS magnitudes and colours have been converted

into the California Institute of Technology (CIT) system. The solid and thick dashed curves represent the unreddened MS and giant branch (Bessell & Brett 1988), respectively. The dotted line indicates the locus of unreddened CTTSs (Meyer et al. 1997). All of the curves and lines are also in the CIT system. The parallel dashed lines are reddening vectors drawn from the tip (spectral type M4) of the giant branch ("upper reddening line"), from the base (spectral type A0) of the MS branch ("middle reddening line") and from the tip of the intrinsic CTTS line ("lower reddening line"). The extinction ratios $A_J/A_V = 0.265$, $A_H/A_V = 0.155$, and $A_K/A_V = 0.090$, have been taken from Cohen et al. (1981). We classified sources according to three regions in this diagram (cf. Ojha et al. 2004a). 'F' sources are located between the upper and middle

Table 7. YSOs identified on the basis of Hα emission, NIR CCD, MIR CCD, MIR CMD, and X-ray emission.*

ID	Radial distance (′)	α_{2000} (h:m:s)	δ_{2000} (°:′:″)	V (mag)	$(V-I)$ (mag)	J (mag)	H (mag)	K_s (mag)	$3.6\,\mu m$ (mag)	$4.5\,\mu m$ (mag)	$5.8\,\mu m$ (mag)	$8.0\,\mu m$ (mag)	Remarks[†]
1	0.07	00:52:39.22	+56:37:49.1	16.095	1.381	13.711	13.035	12.943	—	—	—	—	3, 2
2	0.44	00:52:42.49	+56:37:55.9	—	—	16.060	15.143	15.056	—	—	—	—	3, 2
3	0.47	00:52:40.56	+56:38:12.1	—	—	15.704	14.813	14.633	—	—	—	—	3, 2
4	0.54	00:52:35.82	+56:37:33.6	17.766	1.674	14.829	13.875	13.289	—	—	—	—	3, 1
5	0.63	00:52:35.19	+56:37:32.7	—	—	15.674	14.854	14.418	—	—	—	—	3, 2
—	—	—	—	—	—	—	—	—	—	—	—	—	—
—	—	—	—	—	—	—	—	—	—	—	—	—	—
—	—	—	—	—	—	—	—	—	—	—	—	—	—

* The radial distance is from the cluster center. The complete table is available in the electronic form only ⟨http://pasj.asj.or.jp/v64/n5/640107/⟩.

[†] 1 = CTTS, 2 = WTTS, 3 = X-ray, 4 = Hα, 5 = Class 0/I, 6 = Class II.

reddening lines, and are considered to be either field stars (MS stars, giants) or Class III and Class II sources with small NIR-excesses. 'T' sources are located between the middle and lower reddening lines. These sources are considered to be mostly CTTSs (or Class II objects) with large NIR-excesses. There may be an overlap of Herbig Ae/Be stars in the 'T' region (Hillenbrand et al. 1992). 'P' sources are those located in the region redward of the lower reddening line, and are most likely Class I objects (protostar-like objects; Ojha et al. 2004a). It is worthwhile to also mention that Robitaille et al. (2006) have shown that there is a significant overlap between proto-stars and CTTSs. The NIR TCD of the NGC 281 region (left panel of figure 6) indicates that a significant number of sources show $(H-K)$ excess; these are shown by open triangles. The sources having X-ray emission and Hα emission are shown by circles (open and filled) and star symbols, respectively. A comparison of the TCD of the NGC 281 region with the NIR TCD of a nearby reference region (right panel of figure 6) indicates that the sources in the NGC 281 region having X-ray emission and lying in the 'F' region above the extension of the intrinsic CTTS locus as well as sources having $(J-H) \geq 0.6$ mag and lying to the left of the first (left-most) reddening vector (shown by filled circles) could be WTTSs/Class III sources. Here, it is worthwhile to mention that some of the X-ray sources classified as WTTSs/Class III sources, lying near the middle reddening vector, could be CTTSs/ Class II sources. The CTTSs and WTTSs identified in this section are listed in table 7.

4.3.2. On the basis of MIR data

The NGC 281 region also has MIR observations through the Spitzer Space Telescope towards the south-west direction of the cluster. Since young stars inside cloud clumps are often deeply embedded, these MIR observations can provide deeper insight into the embedded YSOs. YSOs occupy distinct regions in the IRAC colour plane according to their nature; this makes MIR TCDs a very useful tool for the classification of YSOs. Whitney et al. (2003) and Allen et al. (2004) presented independent model predictions for IRAC colours of various classes of YSOs. Figure 7 (left) presents a $[5.8]-[8.0]$ versus $[3.6]-[4.5]$ TCD for the observed sources. The sources within the box represent the location of Class II objects (Allen et al. 2004; Megeath et al. 2004). The sources located around $[5.8]-[8.0]=0$ and $[3.6]-[4.5]=0$ are fore-ground/background stars as well as Class III objects. Sources

with $[3.6]-[4.5] \geq 0.8$ and/or $[5.8]-[8.0] \geq 1.1$ have colours similar to those derived from models of protostellar objects with in-falling dusty envelopes (Allen et al. 2004). These are Class 0/I sources. Encircled objects represent sources with X-ray emission. A majority of the Class II objects have X-ray emission, whereas none of the Class 0/I sources show X-ray emission. It is found that four of the probable Class 0/I sources identified on the basis of MIR data lie in the unexposed area of the detector (ACIS-I) of the Chandra telescope, whereas one lies near the edge of detector ACIS-I of the Chandra telescope.

The detection of Class 0/I and Class II sources in all four IRAC bands is limited mainly by the lower sensitivity of the 5.0 and 8.0 μm channels. Figure 7 (right panel) shows the IRAC colour–magnitude diagram (CMD) for stars detected in the 3.6 and 4.5 μm bands. Encircled objects represent sources with X-ray emission. Stars having $0.35 \leq [3.6]-[4.5] \leq 0.80$ mag could be probable Class II stars, whereas stars having $[3.6]-[4.5] > 0.80$ could be Class 0/I sources. As can be seen, a majority of the Class II sources are X-ray emit-ting stars, whereas X-ray emission is mostly absent in probable Class 0/I sources. One of the critical astrophysical questions is whether X-ray emission is present in Class 0/I sources at the very onset of star formation when collimated outflows begin (Getman et al. 2007). A few studies report the detection of X-rays from Class 0/I protostars, whereas some studies have reported that many bona-fide protostars are not detected in X-ray images (cf. Tsuboi et al. 2001; Hamaguchi et al. 2005; Getman et al. 2007). The non-detection of X-ray emission in Class 0/I sources is usually attributed to heavy obscuration instead of the intrinsic absence of X-ray emission in protostars. The sources having colours $0.35 \leq [3.6]-[4.5] \leq 0.80$ mag and X-ray emission are considered as Class II sources; these are also listed in table 7.

To further elucidate the nature of the PMS sources, we derived SEDs for 35 sources (cf. table 8) using optical, NIR, and MIR photometry. In figure 8, we show a sample of three SEDs for three different classes. To classify the evolutionary stage of YSOs using the SEDs, we adopted the classification scheme of Lada et al. (2006), which defines the spectral class index $\alpha = d\log(\lambda F_\lambda)/d\log(\lambda)$. We computed the spec-tral class index, $\alpha_{K-8\mu m}$, which is the slope of the linear fit to the fluxes at the K_s and IRAC 8 μm bands. Objects with $\alpha_{K-8\mu m} \geq +0.3$, $+0.3 > \alpha_{K-8\mu m} \geq -0.3$, $-0.3 > \alpha_{K-8\mu m} \geq -1.8$, and $-1.8 > \alpha_{K-8\mu m}$ are considered to be Class I,

Table 8. MIR, NIR, and optical data for Class 0/I, Class II, and Class III objects as detected on the basis of MIR TCD (cf. subsection 5).

| ID	α_{2000} (h: m: s)	δ_{2000} (°: ′: ″)	3.6 μm (mag)	4.8 μm (mag)	5.8 μm (mag)	8.0 μm (mag)	J (mag)	H (mag)	K_s (mag)	V (mag)	$U-B$ (mag)	$B-V$ (mag)	$V-I$ (mag)	X-rays Y/N	ID (table 7)
Class 0/I															
Ia	00:52:10.99	+56:30:58.8	9.873	7.856	6.002	4.992	17.235	15.499	14.854	—	—	—	—	—	213
Ib	00:52:11.76	+56:33:04.5	10.409	9.175	8.023	7.113	17.067	15.439	13.445	—	—	—	—	—	181
Ic	00:52:29.97	+56:33:29.2	11.129	9.372	8.114	7.114	—	—	—	—	—	—	—	—	123
Id	00:52:17.15	+56:33:42.5	11.678	9.538	7.937	6.846	—	—	—	—	—	—	—	—	137
Ie	00:52:26.58	+56:33:25.5	11.845	10.677	9.793	9.170	17.614	17.246	14.904	—	—	—	—	—	127
If	00:52:24.56	+56:33:50.1	12.175	10.345	9.668	9.714	—	—	—	—	—	—	—	—	121
Ig	00:52:13.48	+56:33:41.4	12.232	11.233	10.323	9.459	18.614	16.133	14.317	—	—	—	—	—	156
Ih	00:52:16.45	+56:31:45.9	12.765	12.256	11.478	10.362	16.519	14.960	13.984	—	—	—	—	—	200
Ii	00:52:15.92	+56:33:49.5	13.065	11.618	10.383	9.644	18.744	16.025	15.401	—	—	—	—	—	139
Ij	00:52:19.56	+56:32:58.4	13.255	12.723	12.101	10.955	15.962	14.941	14.371	—	—	—	—	—	164
Ik	00:52:32.54	+56:32:33.6	13.401	12.822	11.557	9.870	16.697	15.463	15.115	19.743	—	—	1.758	—	149
Il	00:52:21.37	+56:30:40.4	13.711	12.544	11.454	10.546	—	—	—	—	—	—	—	—	209
Im	00:52:25.55	+56:33:32.6	15.221	13.185	11.631	10.246	—	—	—	—	—	—	—	—	126
In	00:52:31.37	+56:33:31.2	15.625	13.613	12.470	11.700	—	—	—	—	—	—	—	—	120
Class II															
IIa	00:52:20.84	+56:33:08.2	10.048	9.305	8.535	7.695	16.288	14.617	12.502	—	—	—	—	Y	147
IIb	00:52:22.39	+56:34:26.5	10.957	10.422	9.871	8.993	14.741	13.121	12.207	—	—	—	—	Y	101
IIc	00:52:12.49	+56:34:13.7	11.148	10.449	9.714	8.798	17.305	14.889	13.359	—	—	—	—	—	141
IId	00:52:27.34	+56:34:03.2	11.345	10.925	10.410	9.629	15.891	14.148	12.973	—	—	—	—	Y	102
IIe	00:52:27.31	+56:32:04.8	11.375	10.583	9.867	9.125	15.832	14.231	13.388	—	—	—	—	—	179
IIf	00:52:35.75	+56:34:31.1	11.391	10.820	10.330	9.896	15.383	13.871	12.827	—	—	—	—	—	71
IIg	00:52:18.83	+56:33:05.9	11.590	11.187	10.813	10.385	14.510	13.390	12.821	—	—	—	—	Y	159
IIh	00:52:19.31	+56:31:14.4	11.814	11.269	10.714	9.967	14.582	13.479	12.947	19.256	—	—	2.708	Y	204
IIi	00:52:21.59	+56:31:31.8	11.947	11.517	11.108	10.427	15.087	13.769	13.031	—	—	—	—	Y	198
IIj	00:52:10.89	+56:34:06.3	12.170	11.634	11.212	10.561	17.328	15.770	14.193	—	—	—	—	—	153
IIk	00:52:33.69	+56:35:59.8	13.010	12.775	12.496	11.841	14.976	14.000	13.657	17.963	—	1.177	1.904	Y	29
IIl	00:52:19.49	+56:32:52.7	13.169	12.694	12.028	11.484	16.189	15.358	14.957	—	—	—	—	—	170
IIm	00:52:14.89	+56:31:44.8	13.885	13.340	12.702	11.638	17.147	15.553	15.261	—	—	—	—	—	202
Class III															
IIIa	00:52:16.82	+56:31:33.4	8.601	8.477	8.431	8.486	8.736	8.556	8.515	12.828	0.027	0.893	1.362	Y	—
IIIb	00:52:10.31	+56:31:31.6	9.252	8.835	8.513	8.192	10.904	10.402	9.974	12.682	0.790	1.145	1.268	—	207
IIIc	00:52:14.65	+56:34:39.6	9.699	9.794	9.634	9.569	10.558	10.000	9.839	13.594	1.090	1.352	1.448	—	—
IIId	00:52:34.26	+56:32:21.0	10.173	10.230	10.200	10.268	11.137	10.449	10.287	10.867	-0.507	0.225	0.362	—	—
IIIe	00:52:36.28	+56:36:00.0	10.271	10.315	10.207	9.944	10.395	10.313	10.334	11.885	0.240	0.467	0.572	—	—
IIIf	00:52:42.88	+56:35:16.3	10.712	10.727	10.642	10.789	10.997	10.835	10.768	13.517	0.549	0.658	0.933	—	—
IIIg	00:52:40.55	+56:35:50.1	11.224	11.236	11.111	11.205	11.859	11.548	11.391	—	—	—	—	Y	—
IIIh	00:52:25.71	+56:34:15.5	11.913	11.300	10.783	10.523	17.138	14.700	13.611	—	—	—	—	Y	95
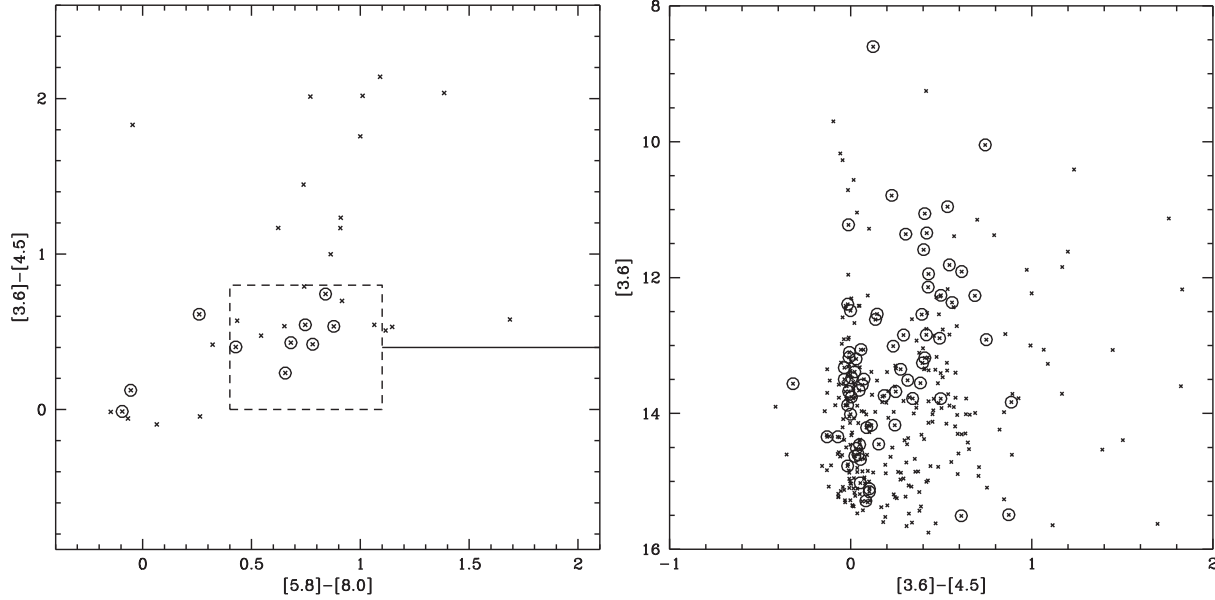
Fig. 7. (left) IRAC MIR TCD of the detected sources. The sources lying within the box are Class II sources. The sources located around $[5.8] - [8.0] \sim 0$ and $[3.6] - [4.5] \sim 0$ are field/Class III stars. The sources with $[3.6] - [4.5] \geq 0.8$ and/or $[5.8] - [8.0] \geq 1.1$ represent Class 0/I objects. The horizontal continuous line shows the adopted division between Class I and Class I/II sources (see Megeath et al. 2004). (right) IRAC CMD for sources detected in the 3.6 and 4.5 μm bands only. Encircled sources represent objects with X-ray emission.
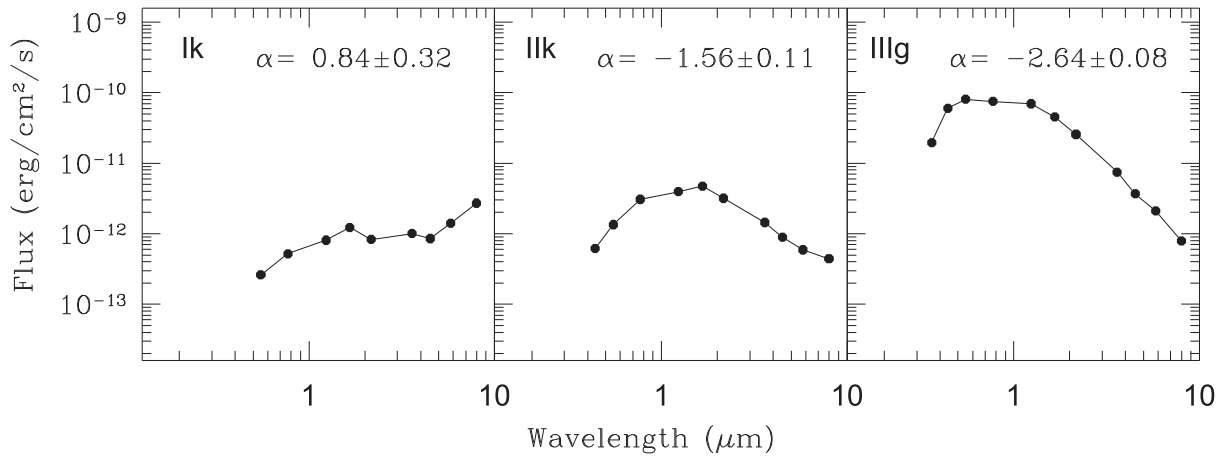
Fig. 8. Sample SEDs obtained by using the optical, NIR, and MIR observations. Stars Ik, IIk, and IIIg represent Class 0/1, Class II, and Class III sources, respectively, classified according to the MIR TCDs (cf. sub-subsection 4.3.2), as given in table 7.

Flat, Class II, and Class III sources respectively. The α indices obtained from the SEDs, in general, confirm the classification obtained from the MIR TCD [cf. figure 7 (left)]. However, the $\alpha_{K-8\mu m}$ indices of two sources (Ih and Ij; Class I on the basis of MIR TCD) reveal that these must be Class II sources, whereas two seemingly Class II sources on the basis of the MIR TCD (IIa and IIc) appear to be Class I sources on the basis of the SEDs. The MIR TCD classifies the two sources, namely IIIb and IIIh as Class III sources, whereas $\alpha_{K-8\mu m}$ indices classify them as Class II objects.

Table 7 provides a complete list of YSOs identified in the present study on the basis of Hα emission, X-ray emission, NIR, and MIR observations. The table contains 12 Hα emission, 134 X-ray emission, 87 NIR excess (CTTSs) sources, and 118 WTTSs. The MIR data yield 25 and 61

Class I and Class II sources, respectively. The $J/(J - H)$ CMD (figure 9) reveals that the identified YSOs are probably PMS stars of age $\lesssim 1$ Myr. The majority of these stars have masses of between 0.5–3.5 $M_{\odot}$.

4.4. Optical Colour–Magnitude Diagram

The $V/(V - I)$ CMD for stars lying within the cluster region is shown in the left-hand panel of figure 10. A more or less well-defined broad MS, presumably due to variable reddening in the cluster region can be noticed down to ~ 15 mag. The distribution of stars fainter than $V \sim 15$–16 mag deviates towards the red side of the MS, indicating the presence of PMS stars in the cluster region. Contamination due to a field star population is also evident in the CMD. To study the LF/MF of the cluster, it is necessary to remove field star contamination
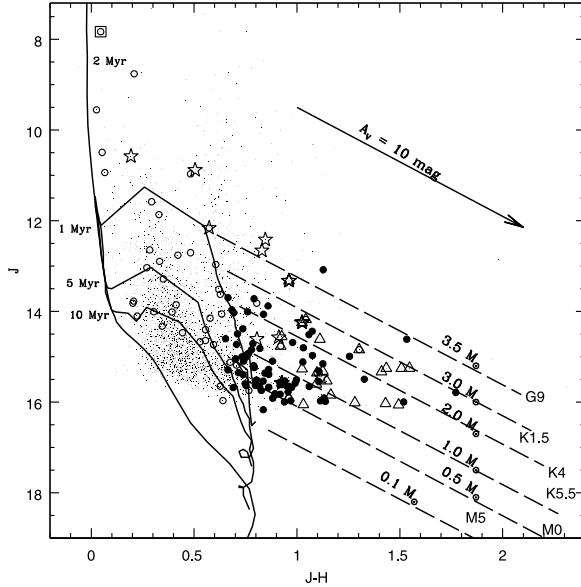
Fig. 9. $J/(J - H)$ CMD of the X-ray sources (open circles), Hα emission stars (star symbols), NIR-excess sources (open triangles), probable WTTSs (filled circles), and an O-type star (open square), having photometric errors of less than 0.1 mag, in the NGC 281 region. The isochrone of 2 Myr ($Z = 0.02$) and PMS isochrones of age 1, 5, and 10 Myr by Marigo et al. (2008) and Siess et al. (2000), respectively, corrected for a distance of 2.81 kpc and reddening $E(B - V)_{min} = 0.32$ mag are also shown. The parallel slanting dashed lines denote loci of 1 Myr old PMS stars having masses in the range of 0.1 to 3.5 $M_{\odot}$, taken from Siess et al. (2000).
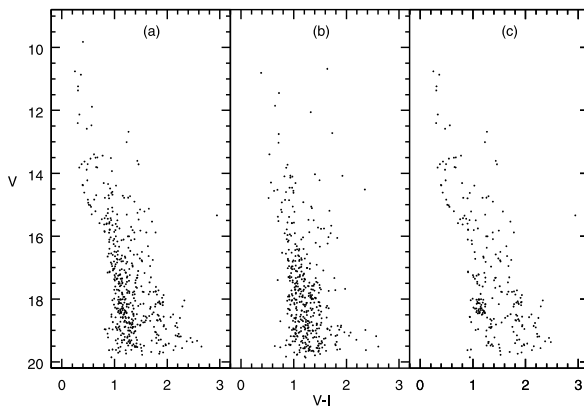
Fig. 10. $V/(V - I)$ CMD for (a) stars in the cluster region and (b) stars in the reference region. (c) is a statistically cleaned CMD.

from the sample of stars in the cluster region because PMS member stars and dwarf foreground stars both occupy similar positions above the ZAMS in the CMD. In the absence of proper motion data, we used a statistical method to estimate the number of probable member stars in the cluster region. We again utilize the reference region towards the north-west (cf. sub-subsection 4.1.2); it has the same area as that of the cluster region. The middle panel of figure 10 shows its $V/(V - I)$ CMD.

To remove contamination due to field stars, we statistically subtracted their contribution from the CMD of the cluster

region using the following procedure. The CMDs of the cluster as well as of the reference region were divided into grids of $\Delta V = 1$ mag by $\Delta(V - I) = 0.4$ mag. The number of stars in each grid of the CMDs were counted. After applying the completeness corrections using the CF (cf. table 2) to both of the data samples, the probable number of cluster members in each grid were estimated by subtracting the corrected reference star counts from the corrected counts in the cluster region. The estimated numbers of contaminating field stars were removed from the cluster CMD in the following manner. For a randomly selected star in the CMD of the reference region, the nearest star in the cluster CMD within $V \pm 0.25$ and $(V - I) \pm 0.125$ of the field was removed. Although the statistically cleaned $V/(V - I)$ CMD of the cluster region shown in figure 10c clearly shows the presence of PMS stars in the cluster, however, the contamination due to field stars at $V \gtrsim 17$ mag and $(V - I) \sim 1.2$ mag can still be seen. This field population could be due to the background population, as discussed by Pandey et al. (2006).

The available distance estimates of NGC 281 in the literature varies from 2.0 kpc to 3.7 kpc (cf. Sato et al. 2008). For further analysis we adopt the VLBI trigonometric distance of the maser source of 2.81 ± 0.24 kpc (Sato et al. 2008). Figure 11 (left panel) shows statistically cleaned dereddened $V_0/(V - I)_0$ CMD, where stars having spectral type earlier than A0 were individually dereddened (cf. subsubsection 4.2.1), whereas the mean reddening of the nearby region, estimated from the available individual reddening values in that region, was used for other stars. We have also plotted the ZAMS by Marigo et al. (2008) and the PMS isochrones by Siess et al. (2000) using a distance of 2.81 ± 0.24 kpc. The evolutionary tracks by Siess et al. (2000) for various masses have also been plotted, which reveal that the majority of YSOs have masses of between 0.5–3.5 $M_{\odot}$. Figure 11 (left panel) indicates an age spread for the PMS population. To check its reality, we plotted $V_0/(V - I)_0$ CMD [assuming a mean $E(B - V) = 0.4$ mag] for the Hα emission stars, NIR-excess stars (probable CTTSs), and X-ray stars (probable WTTSs) (cf. subsection 4.3) in figure 11 (right panel). This also indicates an age spread of about 1–5 Myr for these probable PMS stars, supporting the reality of that in figure 11 (left panel).

The age and mass of each YSO were estimated by comparing its location with the isochrones. Here, we would like to point out that the estimation of the ages and masses of the PMS stars by comparing their positions in the CMDs with the theoretical isochrones is prone to random as well as systematic errors (see e.g., Hillenbrand 2008; Hillenbrand et al. 2008; Chauhan et al. 2009, 2011). Chauhan et al. (2009) and Barentsen et al. (2011) have studied the effect of random errors in the age estimation of PMS stars. Barentsen et al. (2011) found that uncertainty in the extinction estimation could play a significant role. In the case of the NGC 281 region, the variable extinction is small (~ 0.2 mag); hence, it should not contribute significantly to the errors. The effect of random error due to a photometric error and reddening estimation in the determination of ages and masses was estimated by propagating the random errors to their observed estimation by assuming a normal error distribution
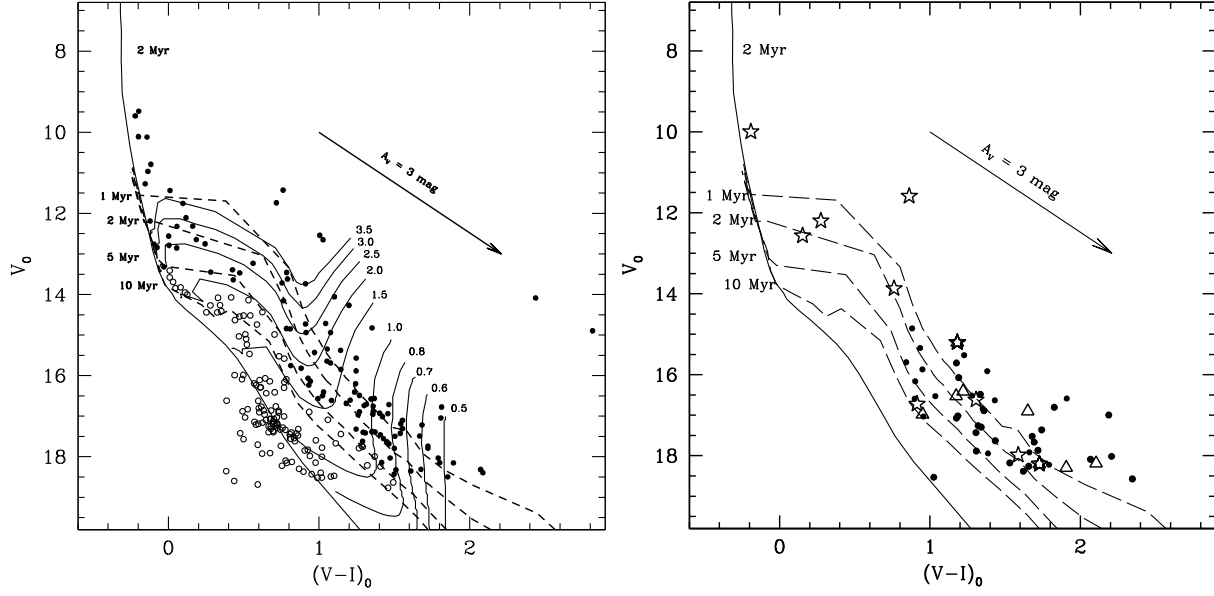
Fig. 11. Statistically cleaned $V_0/(V-I)_0$ CMD for stars lying in the cluster region (left panel). Filled circles (Ages ≤ 5 Myr) are used to estimate the MF of the region. The right panel shows the $V_0/(V-I)_0$ CMD for the Hα emission stars (star symbols), NIR-excess stars (triangles), and X-ray sources in the 'F' region of the NIR TCD (solid circles) (see subsection 4.3 for details) collectively. The ZAMS by Marigo et al. (2008) and the PMS isochrones of 1, 2, 5, 10 Myr along with evolutionary tracks for different mass by Siess et al. (2000) are also shown. All of the curves are corrected for a distance of 2.81 kpc.

Table 9. The mass and age of the YSOs having optical counterparts along with the associated errors.[*]

ID	Mass $\pm \sigma$ ($M_\odot$)	Age $\pm \sigma$ (Myr)	ID	Mass $\pm \sigma$ ($M_\odot$)	Age $\pm \sigma$ (Myr)	ID	Mass $\pm \sigma$ ($M_\odot$)	Age $\pm \sigma$ (Myr)
1	2.20 ± 0.11	1.01 ± 0.21	48	1.15 ± 0.07	0.58 ± 0.09	192	0.35 ± 0.02	0.37 ± 0.27
4	1.11 ± 0.08	1.36 ± 0.30	50	0.52 ± 0.03	0.72 ± 0.06	197	0.53 ± 0.04	0.42 ± 0.16
6	0.84 ± 0.05	0.68 ± 0.09	51	0.57 ± 0.05	1.89 ± 0.51	199	0.96 ± 0.07	0.34 ± 0.04
7	2.72 ± 0.13	3.09 ± 0.39	53	0.89 ± 0.07	2.19 ± 0.55	201	0.45 ± 0.03	1.01 ± 0.12
8	0.53 ± 0.05	2.10 ± 0.61	59	0.36 ± 0.01	0.31 ± 0.23	206	0.34 ± 0.01	0.10 ± 0.01
9	6.29 ± 0.30	0.36 ± 0.04	60	1.08 ± 0.06	0.43 ± 0.05	209	5.34 ± 0.07	0.17 ± 0.02
12	1.84 ± 0.10	1.19 ± 0.24	63	0.54 ± 0.04	1.45 ± 0.34	214	0.81 ± 0.06	3.10 ± 0.71
14	0.72 ± 0.07	0.67 ± 0.10	65	0.82 ± 0.04	0.92 ± 0.12	217	0.44 ± 0.01	0.10 ± 0.00
18	0.97 ± 0.08	3.71 ± 0.97	67	0.91 ± 0.06	3.96 ± 0.82	220	1.48 ± 0.03	4.86 ± 0.29
22	0.65 ± 0.05	2.20 ± 0.58	70	1.87 ± 0.05	2.79 ± 0.57	221	1.70 ± 0.04	3.82 ± 0.68
23	0.73 ± 0.07	1.69 ± 0.40	75	0.53 ± 0.03	1.01 ± 0.14	227	1.43 ± 0.03	4.85 ± 0.27
25	3.31 ± 0.14	1.66 ± 0.27	76	1.09 ± 0.06	0.77 ± 0.12	228	0.94 ± 0.03	5.00 ± 0.00
27	1.66 ± 0.08	1.91 ± 0.40	79	0.79 ± 0.03	5.00 ± 0.00	229	3.10 ± 0.09	0.96 ± 0.25
29	0.75 ± 0.05	0.77 ± 0.07	80	1.11 ± 0.07	2.67 ± 0.62	230	0.59 ± 0.04	1.38 ± 0.27
30	0.84 ± 0.06	1.59 ± 0.34	85	1.14 ± 0.03	4.99 ± 0.03	231	0.82 ± 0.04	0.41 ± 0.03
31	0.49 ± 0.03	0.87 ± 0.09	87	1.09 ± 0.07	2.37 ± 0.53	233	1.22 ± 0.07	0.39 ± 0.04
32	0.92 ± 0.06	0.85 ± 0.15	88	0.73 ± 0.05	1.24 ± 0.18	234	0.87 ± 0.03	5.00 ± 0.00
34	0.51 ± 0.03	0.78 ± 0.07	90	0.87 ± 0.05	1.67 ± 0.34	235	0.64 ± 0.04	4.48 ± 0.72
36	0.60 ± 0.04	0.80 ± 0.15	96	1.39 ± 0.05	2.74 ± 0.55	236	0.52 ± 0.02	0.10 ± 0.00
38	1.64 ± 0.04	3.41 ± 0.65	108	0.79 ± 0.05	1.68 ± 0.29	242	0.40 ± 0.02	0.91 ± 0.08
40	0.49 ± 0.01	0.10 ± 0.01	125	0.88 ± 0.05	0.85 ± 0.14	245	0.49 ± 0.04	1.12 ± 0.18
43	0.81 ± 0.04	0.95 ± 0.13	149	0.78 ± 0.03	5.00 ± 0.01	250	0.35 ± 0.01	0.30 ± 0.23
44	1.34 ± 0.03	4.96 ± 0.05	150	0.78 ± 0.03	5.00 ± 0.01	259	1.03 ± 0.06	0.97 ± 0.16
45	0.90 ± 0.05	4.39 ± 0.72	169	1.04 ± 0.03	5.00 ± 0.00	268	0.82 ± 0.03	5.00 ± 0.00
46	0.73 ± 0.05	1.61 ± 0.27	175	0.30 ± 0.01	0.12 ± 0.06			
47	0.48 ± 0.03	0.57 ± 0.11	187	1.32 ± 0.03	4.97 ± 0.04			

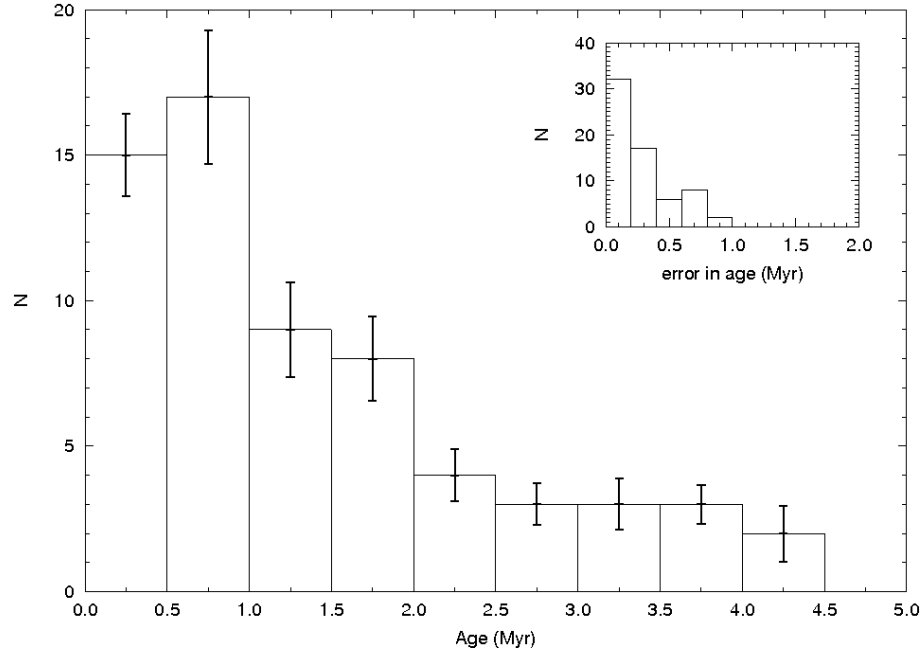[*] The ID is as same as in table 7.

Fig. 12. Histogram showing the distribution of ages of the YSOs. The inset shows the distribution of random errors. The error bar on the Y-axis represents the amount of scatter in each bin estimated on the basis of errors associated with age estimates, as given in table 9, and using Monte Carlo simulations.

and using Monte Carlo simulations. The estimated ages and their error are given in table 9. The systematic errors could be due to the use of different PMS evolutionary models and an error in the distance estimation etc. Barentsen et al. (2011) mentioned that the ages may be incorrect by a factor of two due to systematic errors in the model. The presence of binaries may be another source of error in the age determination. Binarity will brighten the star, and consequently the CMD will yield a lower age estimate. In the case of an equal-mass binary, we expect an error of $\sim 50\%$–60% in the PMS age estimation. However, it is difficult to estimate the influence of binaries/variables on the mean age estimation, since the fraction of binaries/variables is not known. In studies of TTSs in the H II region IC 1396, Barentsen et al. (2011) presumed that the number of binaries in their sample of TTSs could be very low, since close binaries lose their disc significantly faster than single stars (cf. Bouwman et al. 2006).

The age distribution of YSOs shown in figure 12 indicates a significant scatter. The inset of figure 12 shows the distribution of random errors. A comparison manifests that the age distribution of YSOs shows a significantly larger scatter than that which could occur due to random errors. Burningham et al. (2005) investigated the effect of photometric variability in the apparent age spreads observed in the CMDs of OB associations. They found that the combination of binarity, photometric uncertainty, and variability could not explain the observed age spread in the CMDs of OB associations. If the effect of unresolved binaries is not significant, we presume that the main reason for the spread in the distribution of YSOs in figure 11 could be due to the spread in the ages of YSOs.

The ages of young clusters are usually derived on dereddened CMDs by comparing the earliest members to post–main-sequence evolutionary tracks if significant evolution has
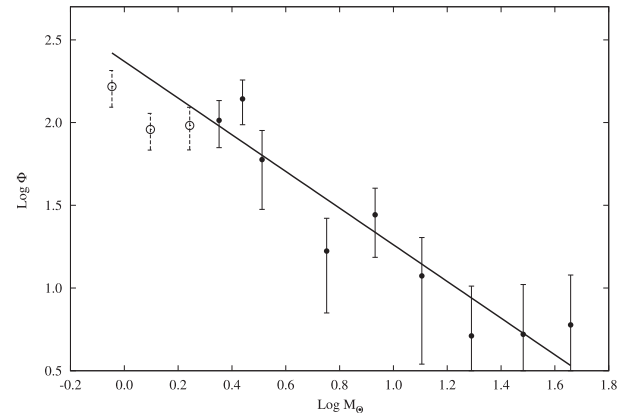
Fig. 13. Plot of the mass function in the cluster. $\log \phi$ represents $\log(N/d \log m)$. The error bars represent the $\pm \sqrt{N}$ errors. The solid line shows the least-squares fit to the mass range $2.0 < M/M_\odot < 54$ (shown by filled circles).

occurred and/or the low mass contracting population to the PMS isochrones. Since the most massive member of the cluster IC 1590 is an O6.5 MS star (Walborn 1973; Abt 1986; Guetter & Turner 1997), its maximum age should be on the order of the MS lifetime of this star, i.e., $\sim 4.4 \, \mathrm{Myr}$ (Meynet et al. 1994). Based also on the PMS stars, Guetter and Turner (1997) derived a maximum age of $\sim 3.5 \, \mathrm{Myr}$ for IC 1590.

We consider the points lying above the 5 Myr isochrone in figure 11 (left panel) as representing the statistics of the PMS stars in the cluster region. Here, we would like to remind the readers that the filled circles in figure 11 may *not* represent the actual members of the cluster. However, they should represent the statistics of PMS stars in the cluster region, and this statistics is used to study its MF only.
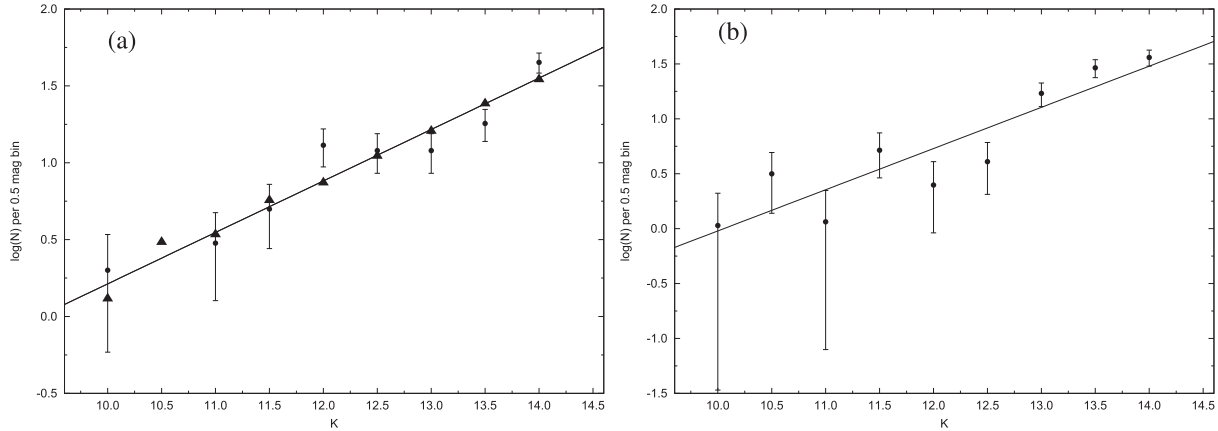
Fig. 14. (a) Comparison of the observed KLF in the reference field and the simulated KLF from the star count modeling. The filled circles denote the observed K-band star counts in the reference region, and the triangles represent the simulation from the galactic model (see the text). The error bars represents the $\pm\sqrt{N}$ errors. The KLF slope (α, see subsection 4.5) of the reference region (solid line) is 0.36 ± 0.05. The simulated model is also gives a similar value of the slope (0.34 ± 0.02). (b) Corrected KLF for the probable members in the cluster (see the text). The straight line is the least-squares fit to the data points in the magnitude range 10.5–14.25. The KLF slope (α) for the cluster region ($R_{\rm cl} < 5'$) is 0.37 ± 0.07.

4.5. Initial-Mass Function and K-Band Luminosity Function

The distribution of stellar masses that form in a star-formation event in a given volume of space is called the initial mass function (IMF). Young clusters are important tools to study the IMF, since they are too young to lose a significant number of members either by dynamical or stellar evolution. The MF is often expressed by a power law, $N(\log m) \propto m^{\Gamma}$, and the slope of the MF is given as

$$\Gamma = d\log N(\log m)/d\log m, \qquad (6)$$

where $N(\log m)$ is the number of stars per unit logarithmic mass interval. The classical value derived by Salpeter (1955) is $\Gamma = -1.35$.

With the help of the statistically cleaned CMD, shown in figure 11 (left panel), we can derive the MF using theoretical evolutionary models. Since the age of the massive cluster members is thought to be ~ 2–4 Myr, stars having $V \lesssim 13$ mag ($V_0 \lesssim 12$ mag; $M \gtrsim 4\,M_{\odot}$) are considered to be still on the MS. For these stars, the LF was converted to a MF using theoretical models by Marigo et al. (2008) (cf. Pandey et al. 2001, 2005). The data for the three brightest stars, which were saturated in the present photometry, were taken from Guetter and Turner (1997). The MF for the PMS stars were obtained by counting the number of stars in various mass bins (shown as evolutionary tracks) having age ≤ 5 Myr in figure 11 (left panel). The resulting MF of the cluster is plotted in figure 13. Since data incompleteness plays an important role in estimating the IMF, we restrict our analysis only to sources having $V < 16.5$ mag. The present data have a completeness of $\sim 95\%$ at $V = 16.5$ mag (cf. table 2). The slope (Γ) of the MF in the mass range $2 < M/M_{\odot} < 54$ turns out to be -1.11 ± 0.15, which seems to be slightly shallower than the Salpeter (1955) value (-1.35). Using various combinations of the maximum expected errors in $E(B-V)$ and the distance, we found that the slope of the MF can vary in the range of -1.08 ± 0.15 to -1.16 ± 0.15. Keeping the errors in the estimation of Γ in mind, it is difficult to decide whether the present slope, 'Γ', is different from that of the Salpeter value. Guetter and Turner (1997) have reported the slope of the MF ($\Gamma = -1.00 \pm 0.21$) for IC 1590 which, within error, is comparable to the value obtained in the present work.

The K-band luminosity function (KLF) is a powerful tool to investigate the IMF of young embedded clusters; therefore, during the last decade, several studies focused on the determination of the KLFs of young open clusters (e.g., Lada & Lada 2003; Ojha et al. 2004b; Sanchawala et al. 2007). In order to obtain the KLF of IC 1590, we again have to examine the effects of incompleteness and field star contamination in our data. The completeness of the data is estimated using the ADDSTAR routine of DAOPHOT, as described in sub-subsection 2.1.1. To take into account the foreground/background field star contamination, we used the Besançon galactic model of stellar population synthesis (Robin et al. 2003), and predicted the star counts in both the cluster region and in the direction of the reference field. We checked the validity of the simulated model by comparing the model KLF with that of the reference field, and found that the two KLFs match rather well (figure 14a). An advantage of using the model is that we can separate the foregrounds ($d < 2.8$ kpc) and the background ($d > 2.8$ kpc) field stars. The foreground extinction towards the cluster region is found to be $A_V \sim 1.0$ mag. Model simulations with $d < 2.8$ kpc and $A_V = 1.0$ give the foreground contamination, and that with $d > 2.8$ kpc and $A_V = 1.7$ mag the background population. We thus determined the fraction of the contaminating stars (foreground+background) over the total model counts. This fraction was used to scale the nearby reference region, and subsequently the modified star counts of the reference region were subtracted from the KLF of the cluster to obtain the final corrected KLF. This KLF is expressed by the following power-law:

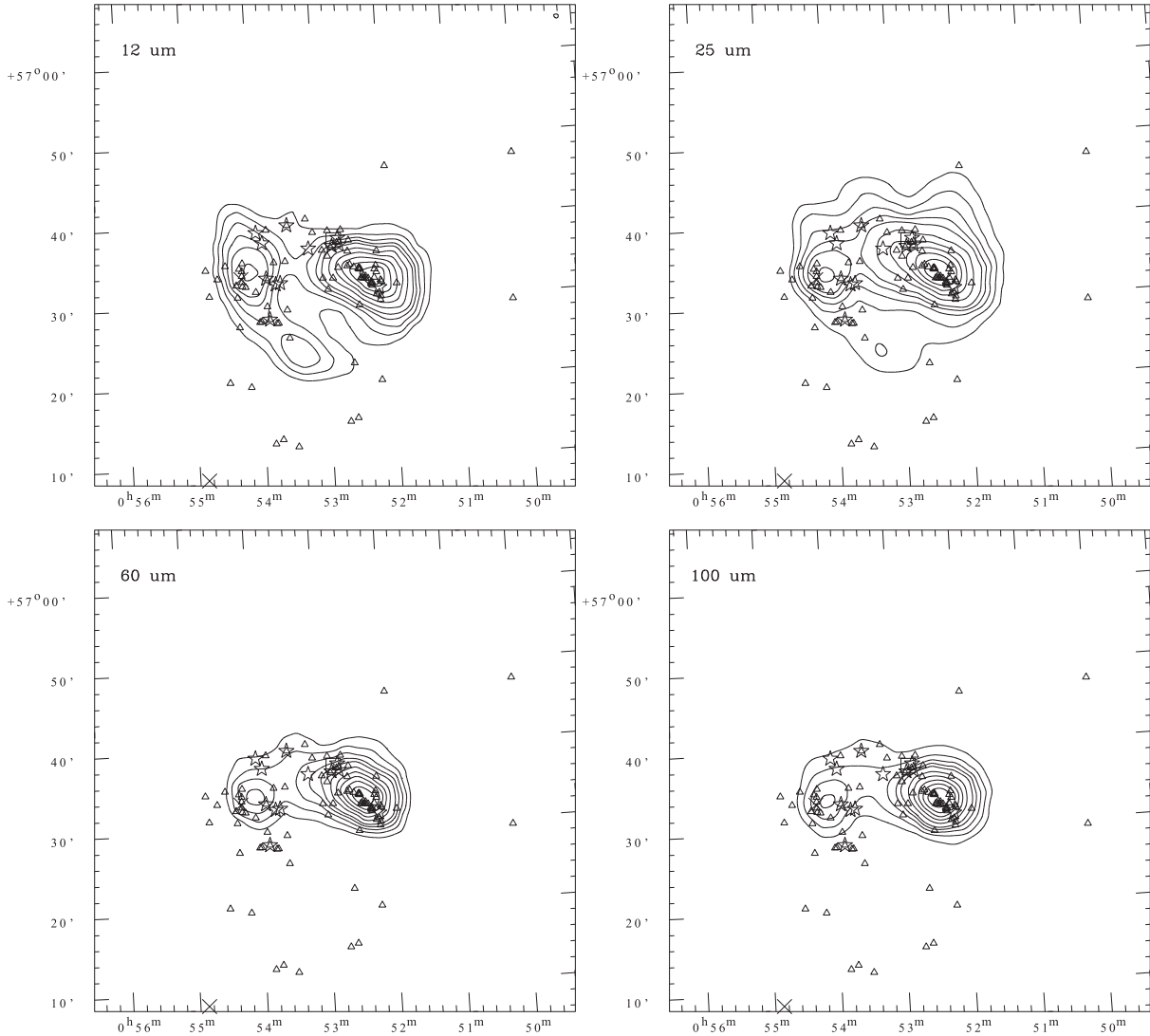$$\frac{dN(K)}{dK} \propto 10^{\alpha K}, \qquad (7)$$

Fig. 15. IRAS intensity maps for the cluster region in 12 μm (top left), 25 μm (top right), 60 μm (bottom left), and 100 μm (bottom right). The contours are at 20%, 25%, 30%, 35%, 40%, 50%, 60%, 70%, 80%, and 90% of the peak value of 20 MJy/s, 48 MJy/s, 412 MJy/s, and 907 MJy/s in 12, 25, 60, and 100 μm respectively. The locations of IR-excess stars (probable CTTSs, triangles), Hα emission stars (star symbols), IRAS point sources (crosses), and the O-type star (open square) are also shown in the image. The abscissa and the ordinate are in the J2000.

where $\dfrac{dN(K)}{dK}$ is the number of stars per 0.5 magnitude bin, and α is the slope of the power law. Figure 14b shows the KLF for the cluster region. This indicates a slope of α = 0.37 ± 0.07, which is similar to the average slopes ($\alpha \sim 0.4$) for young clusters (Lada et al. 1991; Lada & Lada 1995, 2003), but higher than the values (0.27–0.31) obtained for Be 59 (Pandey et al. 2008) and Stock 8 (Jose et al. 2008).

5. Star Formation Scenario

The star-forming region NGC 281 has been attracting attention of the star-forming community. It contains a cluster, IC 1590, with a Trapezium-like system of O-type stars at the center. The ionized hydrogen seems to be associated with two CO molecular clumps (east and west), which were mapped in

^{12}CO and ^{13}CO by Elmegreen and Lada (1978), Leisawitz, Bash, and Thaddeus (1989), Henning et al. (1994), Megeath and Wilson (1997), and Lee and Jung (2003). The western CO clump, called NGC 281 West, is somewhat more massive and compact than the elongated eastern clump (NGC 281 East) (Lee & Jung 2003).

The ionizing source, HD 5005, lies to the northeast/ northwest of NGC 281 West/NGC 281 East. The differential extinction towards the central cluster is ~ 0.2 mag (cf. subsection 4.2.1), indicating that the central cluster contains only gas and dust of low-density. A similar trend has been noticed in many clusters associated with H II regions (e.g., 30 Dor: Brandl et al. 1996; NGC 3603: Pandey et al. 2000; and NGC 1893: Sharma et al. 2007). A reasonable explanation for this lack of a dense medium in the central region may be the effects of the massive star(s) at the cluster center.
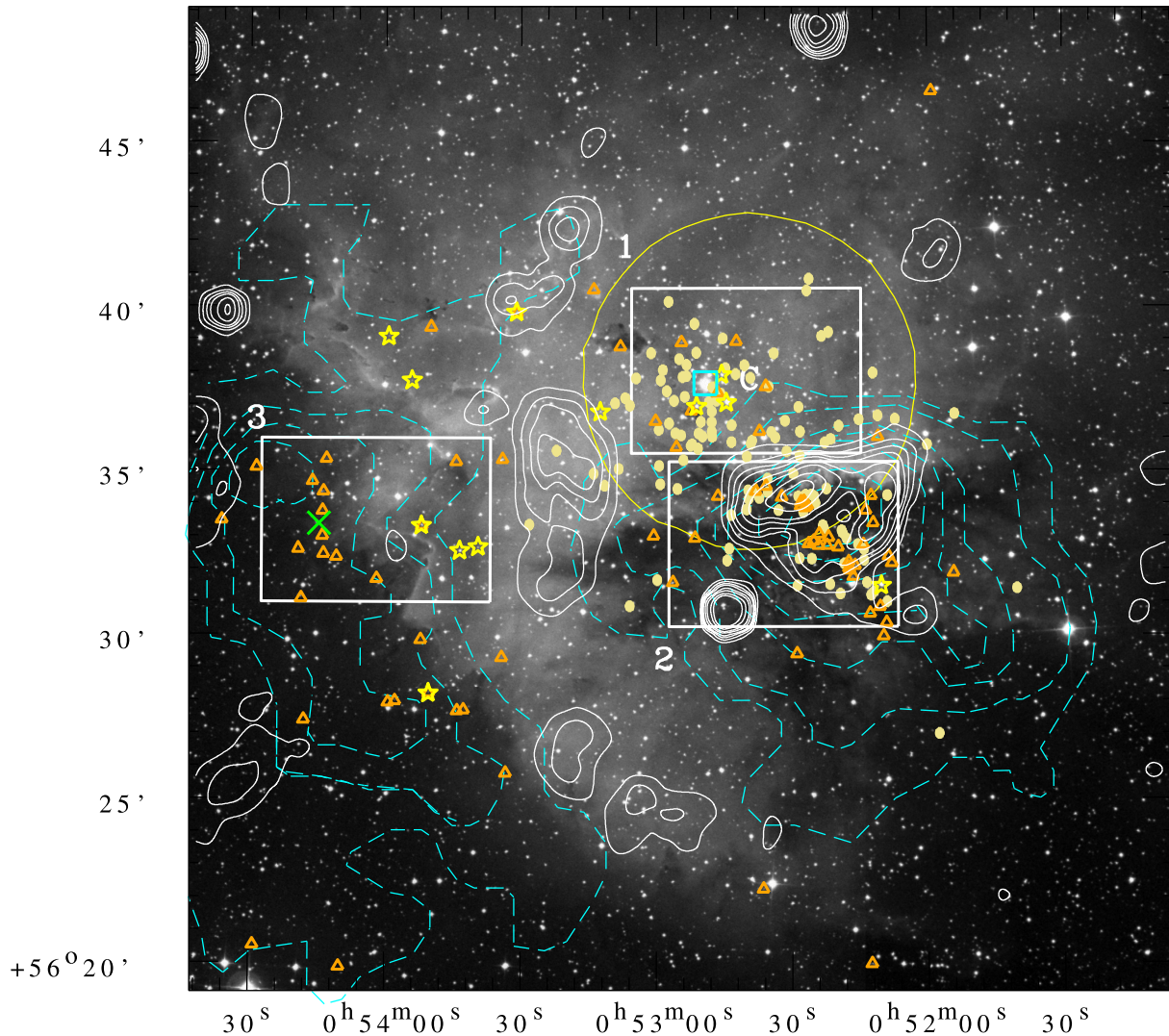
Fig. 16. Locations of IR-excess stars (probable CTTSs, triangles), Hα emission stars (star symbols), IRAS point sources (crosses), the O-type star (open square), and WTTS (filled circles) are overlaid on the DSS-2 *R* band $30' \times 30'$ image. The cluster region is represented by the circle having the center "C". The CO contours taken from Henning et al. (1994) are shown by the blue dashed lines and the NVSS (1.4 GHz) radio continuum contours by white lines. The radio contours are 5%, 10%, 15%, 20%, 30%, 40%, 60%, 80% of the peak value of 0.04 Jy/Beam. Three subregions are also marked by boxes. The abscissa and the ordinate are in J2000.

As indicated in previous studies (cf. Lee & Jung 2003 and references therein), the western molecular clump is interacting with the ionized gas. On the basis of kinetic evidence, Elmegreen and Moran (1979) suggested the passage of a shock through NGC 281 West. An H_2O maser was found to be coincident with the peak of the cloud, indicating ongoing star formation (Elmegreen & Lada 1978). Carpenter et al. (1993) and Megeath (1994) detected a cluster of low-mass stars associated with NGC 281 West. Elmegreen and Lada (1978) suggested that this region is a site of triggered star formation through the "collect and collapse" mode. However, Megeath and Wilson (1997) claimed that numerical models of imploding spherical clumps can approximately reproduce the kinematic features observed in NGC 281 West, and suggested that "radiation-driven implosion" (RDI) is a more plausible and attractive model. Between NGC 281 East and the central cluster a few bright-rimmed clouds (BRCs) or cometary globules and an

IRAS source are located. Some of the Hα stars can be seen around the tip of the BRCs just as observed in several well-known BRCs (see Ogura et al. 2002). Both of the CO clumps show the presence of YSOs (IR-excess and Hα stars) around their respective centers.

Whatever the star-formation scenario, the ionization/shock fronts caused by high-mass stars of the first generation appears to have initiated the formation of a new generation of stars at the edge of the molecular clumps. The distribution of YSOs and morphological details of the environment around the cluster can be used to infer the star-formation history of the NGC 281 region in detail. To know the distribution of YSOs in the region, we included all of the detected YSOs without considering their photometric errors to improve the sample.

IRAS maps can be used to study the distribution of dust and unidentified infrared band (UIB) carriers. Figure 15 shows IRAS intensity maps for the NGC 281 region at 12 μm
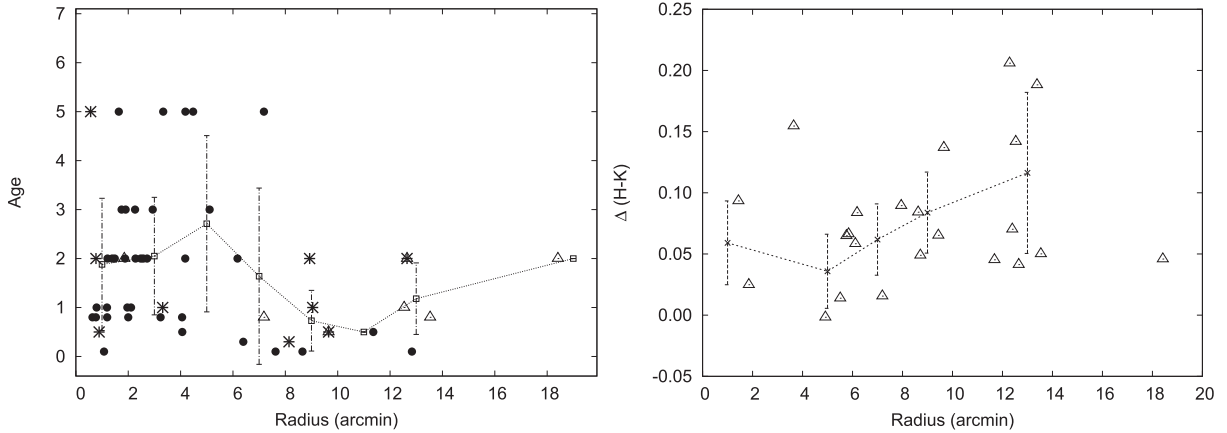
Fig. 17. Variation in the age and NIR-excess [$\Delta(H-K)$] of the YSOs as a function of the radial distance from the O star, HD 5005. The symbols are the same as in figure 6. The dotted line represents the Mean $\pm \sigma$ of the distribution.

(top left), 25 μm (top right), 60 μm (bottom left), and 100 μm (bottom right). The global features of these maps are quite similar to that of the molecular gas. All of the contours show peaks around both the eastern and western clumps, indicating the coexistence of warm dust (IRAS 12 and 25 μm), cold dust (IRAS 60 and 100 μm), and molecular gas. NGC 281 East lacks radio continuum emission, and its extended distribution of the 12 μm emission towards the south resembles that of the molecular material. As pointed out by Leisawitz, Bash, and Thaddeus (1989), in the case of the eastern clump, peak of ionized gas (as seen from the ionized source) is followed by peaks of IR emission and CO emission from the molecular cloud, respectively. The coincidence of the peak of the IRAS and CO emission, the location of the IRAS point source, and the distribution of YSOs indicates ongoing star-formation activity in these clumps.

Figure 16 shows a map of the ^{12}CO emission taken from Henning et al. (1994) and the 1.4 GHz radio emission from NVSS along with the spatial distribution of all the detected YSOs overlaid on the DSS-2 R band image. The center of the cluster IC 1590 is marked by 'C', and the location of the ionization source is shown by a square. A well-aligned distribution of the detected YSOs from the vicinity of the ionization source to the direction of NGC 281 West can be noticed. This spatial distribution of the YSOs resembles that in the case of NGC 1893 and BRC 14, where a similar distribution of NIR-excess stars can be noticed from the ionization source to the direction of the cometary globules/BRC (see figure 22 of Sharma et al. 2007 and figure A3 of Chauhan et al. 2009). These alignments in NGC 1893 and BRC 14 were attributed to triggered star formation due to a series of the RDI process. In both cases, YSOs located away from the ionization sources were found to be younger. Sicilia-Aguilar et al. (2004) have also shown that in the case of the Tr 37/IC 1396 globule region, CTTSs are aligned from the iosizing source towards the direction of the globule, and that most of the younger (~ 1 Myr) members appear to lie near or within the globule. They mentioned that it can be indicative of triggered star formation. Figure 17 (left panel) shows the age distribution of the YSOs as a function of the radial distance from HD 5005, the ionization source of NGC 281, which shows that the YSOs in the

cluster region ($r \lesssim 8'$) have ages $\lesssim 5$ Myr, whereas those lying outside the cluster region are relatively younger, and have ages $\lesssim 2$ Myr. Figure 17 (right panel) shows the radial variation of the NIR-excess $\Delta(H-K)$, which is defined as the horizontal displacement from the middle reddening vector at the boundary of the 'F' and 'T' regions (see figure 6). To quantify the radial variation of the age and NIR-excess, we used only those stars that have an error of ≤ 0.1 mag. The distribution of $\Delta(H-K)$ also suggests that the sources lying outside the boundary of the cluster ($r \sim 8'$) have relatively larger NIR excess compared to those located within the cluster region. However, we admit that the above statements are not conclusive in view of the fact that the scatters are large and the differences are subtle. Deeper optical, NIR, and MIR observations are needed to achieve a conclusive star-formation scenario in the region. A similar trend has been reported in the case of a few BRCs by Chauhan et al. (2009) as well as in a recent study on the IC 1396 region by Barentsen et al. (2011).

The near-IR excess in the case of CTTSs suggests the presence of dusty optically thick discs (Haisch et al. 2001a; Sicilia-Aguilar et al. 2006). Sicilia-Aguilar et al. (2006) found similarities between the decrease in the IR excesses and the decrease in the accretion rates, and concluded that gas evolution seems to somehow occur parallel to the evolution of the dust grains and the structure of the disc. In a recent study, Sicilia-Aguilar et al. (2009) further confirmed that the IR-excess decreases with age. Hence, a relatively large NIR excess outside the cluster region (cf. figure 17, right panel) could be indicative of relatively younger population outside the cluster region.

To study the evolutionary stages of the NGC 281 region, we have divided it into three sub-regions, as shown in figure 16, namely Region 1 (IC 1590), Region 2 (NGC 281 West), and Region 3 (NGC 281 East). Figures 18 and 19 show the $V/(V-I)$ CMDs and NIR TCD, respectively, for the three regions. Here, also we used only sources of good quality, i.e., sources having an error of less than 0.1 mag. X-ray data are not available for Region 3. The CMDs indicate that the age of the YSOs in Region 1 ranges between $\lesssim 1$–5 Myr, whereas a majority of the YSOs in Region 2 have ages < 1 Myr. The YSOs associated with Region 3 indicate an age of ~ 1–2 Myr
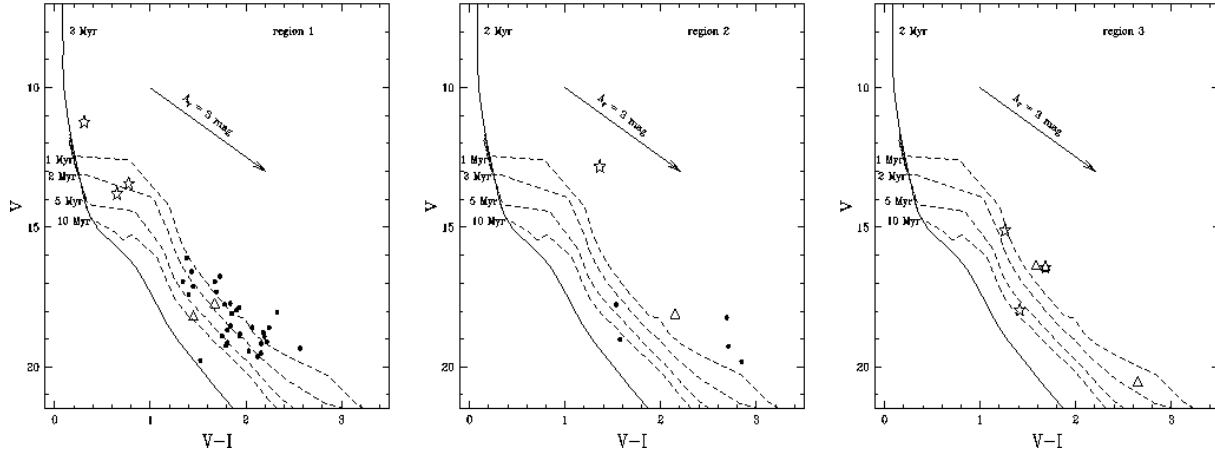
Fig. 18. $V/(V − I)$ CMDs for the probable YSOs detected in three subregions. The symbols are the same as in figure 6. The isochrone for 2 Myr (continuous curve) by Marigo et al. (2008) and the PMS isochrones (dashed curves) for ages 1, 2, 5, 10 Myr by Siess et al. (2000) are also shown. All of the isochrones are corrected for reddening $[E(B − V)_{min} = 0.32\,mag]$ and a distance of 2.81 kpc.
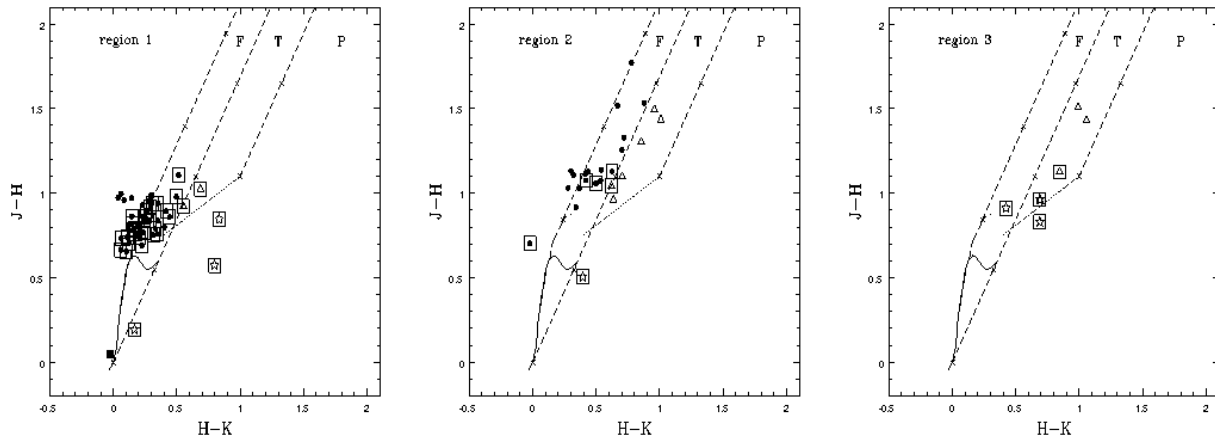

Fig. 19. NIR TCDs of the YSO candidates in the three subregions. The sequences for dwarfs (solid curve) and giants (thick dashed curve) are taken from Bessell and Brett (1988). The dotted line represents the loci of unreddened T Tauri stars (Meyer et al. 1997). Dashed straight lines represent the reddening vectors (see the text). The crosses on the dashed lines are separated by $A_V = 5\,mag$. Open squares show the data having optical counterparts used in figure 18. The other symbols are as the same as in figure 6.

Table 10. Statistics of probable CTTSs in three sub-regions.[*]

Region	Total stars	NIR-excess stars	Hα stars	Probable CTTSs (NIR-excess + Hα stars)	$\Delta (H − K)$ (mag)	A_V (mag)
Stars with error less than 0.1 mag						
1	168	2 (2.5)	3 (3.8)	5 (6.3)	0.06 ± 0.03	1.6 ± 0.2
2	107	6 (33.3)	1 (5.5)	7 (38.9)	0.08 ± 0.04	3.9 ± 1.9
3	97	4 (50.0)	3 (37.5)	6 (75.0)[†]	0.16 ± 0.05	3.6 ± 2.3
Field	89	—	—	—	—	—
All stars independent of errors						
1	425	8 (3.3)	3 (1.3)	11 (4.6)	0.12 ± 0.08	2.5 ± 1.8
2	313	32 (25.2)	1 (0.7)	33 (26.0)	0.10 ± 0.07	4.4 ± 2.8
3	241	12 (21.8)	3 (5.5)	14 (25.5)[†]	0.11 ± 0.07	4.6 ± 2.8
Field	186	—	—	—	—	—

[*] Numbers given in parentheses are in percentage.
[†] One Hα star has NIR-excess.

Table 11. CTTS fraction $f_{\mathrm{CTTS}} = N_{\mathrm{CTTS}}/(N_{\mathrm{CTTS}} + N_{\mathrm{WTTS}})$.

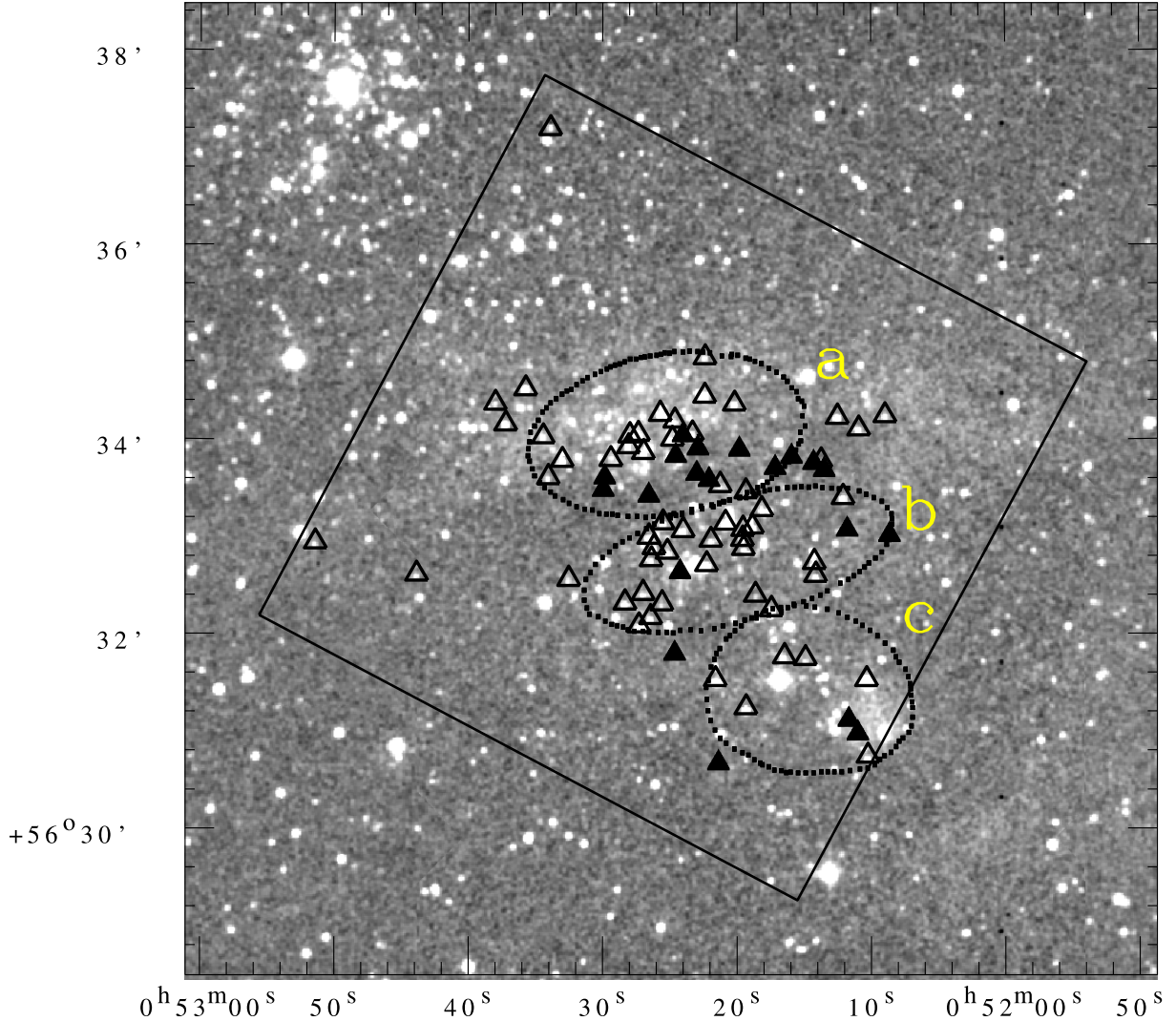| Region	CTTS		WTTS		f_{CTTS}	
	error ≤ 0.1	all	error ≤ 0.1	all	error ≤ 0.1	all
1	2	8	38	56	0.05	0.12
2	6	32	18	39	0.25	0.45

Fig. 20. Spatial distribution of the Class 0/I (filled triangles) and Class II (open triangles) sources detected by Spitzer IRAC overlaid on the 2MASS image of the NGC 281 region. The square box represents the area observed by the Spitzer IRAC. The dashed curves indicate the boundaries of the three sub-clusters, named as a, b, and c (see section 5 for details).

for the region. The NIR TCDs (figure 19) indicate that the extinction in Regions 2 and 3 is relatively higher in comparison to Region 1.

A comparison of the statistics of the YSOs in these three regions can also give a clue about the evolutionary stages of the regions. Table 10 gives statistics of the probable CTTSs associated with the three sub-regions. We have given statistics for those sources having an error of ≤ 0.1 mag as well as for all of the detected YSOs without considering their errors. The total number of stars detected in the 2MASS

Catalogue and the number of field stars expected in each region, estimated from a nearby reference region (cf. subsubsection 4.1.2), are also given in table 10. The percentage of Hα stars and NIR excess stars in each region was estimated after substracting the contribution of the expected field stars (89 stars, column 2 of table 10) from the total stars (also given in column 2 of table 10) in the subregions. The fraction of detected CTTSs (i.e., NIR-excess stars and Hα stars), for both the samples, is significantly higher in Regions 2 and 3 as compared to the cluster region (Region 1). This is further

supported by a comparison of the CTTSs fractions, f_{CTTS} = $N_{\mathrm{CTTS}}/(N_{\mathrm{CTTS}} + N_{\mathrm{WTTS}})$ in Region 1 (5%–12%) and Region 2 (25%–45%) (cf. table 11). The sources flagged as 1 and 2 in column 14 of table 7 are classified as CTTSs and WTTSs, respectively. The WTTSs were identified using the NIR TCD and X-ray data (cf. sub-subsection 4.3.1). X-ray data are not available for Region 3. Here, it is important to mention that as mentioned in sub-subsection 4.3.1, some of the CTTSs having less, or negligible, NIR excess might have been classified as WTTSs. If this is true, the f_{CTTS} will have further higher value. Haisch et al. (2001b) have found the disc evolution fraction in the sense that the fraction of stars having a disc decreases with age. Armitage et al. (2003) have also found that, in Taurus–Auriga T-association, f_{CTTS}, decreases with the stellar age. A comparison of the disc fractions of Regions 1 and 2 with those given by Haisch et al. (2001b) and Armitage et al. (2003) suggested ages of $\sim$ 4–5 Myr and $\sim$ 1–3 Myr for Regions 1 and 2, respectively, which is in fair agreement with results obtained from the CMDs. Thus, the above discussions suggest the propagation of (triggered) star formation in Regions 2 and 3.

Megeath and Wilson (1997) pointed out the presence of two sub-clusters (northern and southern) in NGC 281 West. They concluded that the northern and southern sub-clusters are indeed physically separate sub-clusters, resulting from distinct star-formation events. Based on the location of the sub-clusters, they concluded that the northern sub-cluster appears to be associated with the NW and NE clumps, whereas the southern sub-cluster seems to be associated with the S clump. The spatial distribution of the Class 0/I and Class II sources detected by Spitzer observations overlaid on the 2MASS image is shown in figure 20. Certainly, the YSOs are found to make two sub-clusters. However, a careful look at this figure also manifests a third sub-clustering. The isodensity contours shown in figure 2 also suggest the presence of three sub-clusters. We have visually marked the boundaries of these sub-clusters, designated as 'a', 'b', and 'c'. Some of the detected YSOs are located outside the boundaries of these sub-clusters. Megeath and Wilson (1997) also found that the northern sub-cluster has higher extinction, as compared to the southern sub-cluster. A comparison of the morphology of the molecular cloud as observed in $C^{18}O$ (2–1) (Megeath & Wilson 1997), and the distribution of YSOs in the 'a' sub-cluster region indicates that 'a' sub-cluster seems to be associated with the NW and NE clumps, as referred by Megeath and Wilson (1997), whereas 'c' sub-cluster seems to be associated with the clump 'S'. Megeath and Wilson (1997) found that clump 'S' (-34 to $-32\,\mathrm{km\,s^{-1}}$) is kinematically and spatially distinct from the NW and NE clumps (-32 to $-29\,\mathrm{km\,s^{-1}}$). The velocity distribution suggests that clump 'S' (i.e., sub-cluster 'c') is relatively near to the observer in comparison to the NW clump 'a'. If we assume that the sub-clusters are not associated with each other, the spatial distribution of the YSOs in the sub-cluster 'a' reveals that the Class II sources are relatively near to the ionizing source compared to the Class 0/I sources. We do not find this trend in the sub-cluster 'b'. The distribution of YSOs in sub-cluster 'c' also shows a similar trend, thought the statistics is poor. The distribution of the YSOs detected by using the IRAC data in the case of a few
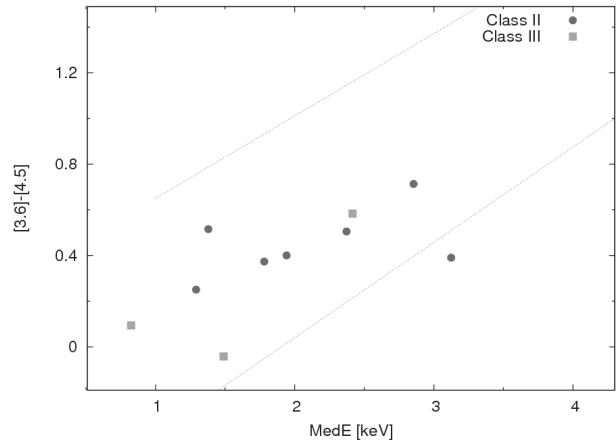

Fig. 21. Spitzer [3.6] − [4.5] MIR colour vs. Chandra X-ray source median energy. Filled circles and squares represent Class II and Class III sources, respectively. The dashed lines indicate the boundaries of the distribution of similar objects in the IC 1396N region (Getman et al. 2007).

BRCs also shows that the Class 0/I sources are found to be located more away from the ionizing sources as compared to Class II sources. This seems to indicate the propagation of star formation in the NGC 281 West region.

6. PMS Sources: MIR and X-Ray Observations

As discussed in sub-subsection 4.3.2, none of the Class 0/I sources show X-ray emission. The high value of A_V in this region could be a possible reason for the non-detection of X-rays in Class 0/I sources. The X-ray median energy (MedE) is a reliable indicator of the absorbing column density through the empirical relation $\log N_{\mathrm{H}} = 21.22 + 0.44\,(\mathrm{MedE})\,\mathrm{cm^{-2}}$ (Feigelson et al. 2005). Getman et al. (2007) have demonstrated a relationship between MedE and the MIR colour [3.6] − [4.5] for obscured PMS stars. Figure 21 shows a MedE vs. [3.6] − [4.5] diagram. The dashed lines represent the boundaries of the distribution obtained in IC 1396 N by Getman et al. (2007, see their figure 8). Using Spitzer photometry, and assuming that the relationship between MedE and MIR colours given by Getman et al. (2007) is valid for the NGC 281 region also, we estimated the MedE for the Class II/III sources detected in the present study as being $\lesssim 4\,\mathrm{keV}$. Using the above relation, the absorbing column densities towards these sources have been estimated to be $N_{\mathrm{H}} \gtrsim 10^{23}\,\mathrm{cm^{-2}}$, which yields $A_V \gtrsim 50\,\mathrm{mag}$ according to the standard gas-to-dust ratio by Ryter (1996). Here, it is interesting to mention that all of the six Class 0/I sources detected in the IC 1396 N region (distance $\sim 0.75\,\mathrm{kpc}$) by Getman et al. (2007) having $A_V \gtrsim 50\,\mathrm{mag}$ show X-ray activity. Non-detection of X-ray emission in probable Class 0/I sources in the NGC 281 region may be due to the detection limit, on account of the larger distance. Deeper exposures are required to reach any conclusions.

7. Summary and Conclusions

In this paper, we present a multiwavelength study of the

NGC 281 region using deep wide-field optical $UBVI_c$ data, and slitless spectroscopy. We also included archival data from surveys, such as Chandra, Spitzer, 2MASS, IRAS, and NVSS. We made an attempt to construct a scenario of global star formation in the NGC 281 complex by taking into account the effects of massive stars on low-mass star formation. The main results from this study are as follow:

- The morphology of the central cluster, IC 1590, is found to be elongated. The extent of the cluster is 6.5 pc and the core radius is 1.6 pc. The maximum age of the ionizing source of the region could be ~ 4 Myr. The minimum reddening $E(B-V)_{\min}$ towards the cluster is estimated to be 0.32 mag, and the cluster shows a small amount of differential reddening, $[E(B-V)] \sim 0.2$ mag. The distribution of the YSOs selected on the basis of NIR-excess, Hα emission, and X-ray emission shows a spread in the CMD. The age distribution of YSOs indicates non-coeval star formation in and around the cluster.

- A slitless spectroscopic survey of the NGC 281 region identifies 12 Hα emission stars. Some of these stars are located near the globules/BRCs, and show the properties of intermediate-low mass PMS stars. On the basis of NIR excess we identified 87 CTTSs. Using a Chandra archival dataset and NIR colour–colour diagram we also identified 118 WTTSs. A majority of the identified YSOs (IR-excess, X-ray, and Hα stars) are low-mass PMS stars having ages $< 1 - \sim 2$ Myr and masses 0.5–3.5 $M_\odot$.

- The slope (Γ) of the MF for the central cluster, IC 1590, in the mass range $2 < M/M_\odot \le 54$ is found to be -1.11 ± 0.15. The slope of the K-band luminosity function (0.37 ± 0.07) is similar to the average value (~ 0.4) reported for young clusters in the literature (i.e., Lada et al. 1991; Lada & Lada 1995, 2003).

- The distribution of gas and dust obtained from the IRAS, CO, and radio continuum maps indicates clumpy structures around the central cluster. The radial distribution, ages, and NIR-excesses $\Delta(H-K)$ of the YSOs as well as the fraction of CTTSs, suggest triggered star formation around the cluster. However, we would like

to caution the readers that the above statement is not conclusive in view of the scatter in the data. Deeper optical, NIR, and MIR observations are needed to have a conclusive view for the star-formation scenario in the region. The Class 0/I and Class II sources detected by using the Spitzer MIR observations indicate that a majority of the Class II sources are X-ray emitting stars, whereas X-ray emission is absent in Class 0/I sources. The spatial distribution of Class 0/I and Class II sources reveals the presence of three sub-clusters in the NGC 281 West region. The distribution of the Class 0/I and Class II sources in the 'a' sub-cluster indicates that the Class II sources tend to be located relatively near to the ionizing source.

References

Abt, H. A. 1986, ApJ, 304, 688

Allen, L. E., et al. 2004, ApJS, 154, 363

Armitage, P. J., Clarke, C. J., & Palla, F. 2003, MNRAS, 342, 1139

Barentsen, G., et al. 2011, MNRAS, 415, 103

Bessell, M. S., & Brett, J. M. 1988, PASP, 100, 1134

Bouwman, J., Lawson, W. A., Dominik, C., Feigelson, E. D., Henning, Th., Tielens, A. G. G. M., & Waters, L. B. F. M. 2006, ApJ, 653, L57

Brandl, B., et al. 1996, ApJ, 466, 254

Brandt, W. N., et al. 2001, AJ, 122, 2810

Broos, P. S., Townsley, L. K., Feigelson, E. D., Getman, K. V., Bauer, F. E., & Garmire, G. P. 2010, ApJ, 714, 1582

Burningham, B., Naylor, T., Littlefair, S. P., & Jeffries, R. D. 2005, MNRAS, 363, 1389

Carpenter, J. M., Snell, R. L., Schloerb, F. P., & Skrutskie, M. F. 1993, ApJ, 407, 657

Chauhan, N., Pandey, A. K., Ogura, K., Jose, J., Ojha, D. K., Samal, M. R., & Mito, H. 2011, MNRAS, 415, 1202

Chauhan, N., Pandey, A. K., Ogura, K., Ojha, D. K., Bhatt, B. C., Ghosh, S. K., & Rawat, P. S. 2009, MNRAS, 396, 964

Chen, W. P., Chen, C. W., & Shu, C. G. 2004, AJ, 128, 2306

Chini, R., Krügel, E., & Kreysa, E. 1990, A&A, 227, L5

Cohen, J. G., Frogel, J. A., Persson, S. E., & Ellias, J. H. 1981, ApJ, 249, 481

Damiani, F., Maggio, A., Micela, G., & Sciortino S. 1997, ApJ, 483, 350

Deharveng L., Zavagno, A., & Caplan J. 2005, A&A, 433, 565

Elmegreen, B. G., & Lada, C. J. 1978, ApJ, 219, 467

Elmegreen, B. G., & Moran, J. M. 1979, ApJ, 227, L93

Feigelson, E. D., et al. 2005, ApJS, 160, 379

Fruscione, A., et al. 2006, Proc. SPIE, 6270, 62701V

Getman, K. V., Feigelson, E. D., Garmire, G., Broos, P., & Wang, J. 2007, ApJ, 654, 316

Guetter, H. H., & Turner, D. G. 1997, AJ, 113, 2116

Haisch, K. E., Jr., Lada, E. A., & Lada, C. J. 2001a, ApJ, 553, 153

Haisch, K. E., Jr., Lada, E. A., & Lada, C. J. 2001b, AJ, 121, 2065

Hamaguchi, K., Corcoran, M. F., Petre, R., White, N. E., Stelzer, B., Nedachi, K., Kobayashi, N., & Tokunaga, A. T. 2005, ApJ, 623, 291

Henning, Th., Martin, K., Reimann, H.-G., Launhardt, R., Leisawitz, D., & Zinnecker, H. 1994, A&A, 288, 282

Hillenbrand, L. A. 2008, in A Decade of Extrasolar Planets around Normal Stars, ed. M. Livio, K. Sahu, & J. Valenti (Cambridge, UK: Cambridge University Press), 84

Hillenbrand, L. A., Bauermeister, A., & White, R. J. 2008, in ASP Conf. Ser., 384, 14th Cambridge Workshop on Cool Stars, Stellar Systems, and the Sun, ed. G. van Belle (San Francisco: ASP), 200

Hillenbrand, L. A., Massey, P., Strom, S. E., & Merrill, K. M. 1993, AJ, 106, 1906

Hillenbrand, L. A., Strom, S. E., Vrba, F. J., & Keene, J. 1992, ApJ, 397, 613

Johnson, H. L. 1966, ARA&A, 4, 193

Johnson, H. L., & Morgan, W. W. 1953, ApJ, 117, 313

Jose, J., et al. 2008, MNRAS, 384, 1675

Kałużny, J., & Udalski, A. 1992, Acta Astron., 42, 29

King, I. 1962, AJ, 67, 471

Lada, C. J., et al. 2006, AJ, 131, 1574

Lada, C. J., & Lada, E. A. 2003, ARA&A, 41, 57

Lada, E. A., Evans N. J., II, Depoy, D. L., & Gatley, I. 1991, ApJ, 371, 171

Lada, E. A., & Lada, C. J. 1995, AJ, 109, 1682

Landolt, A. U. 1992, AJ, 104, 340

Lee, Y., & Jung, J.-H. 2003, New Astron., 8. 191

Leisawitz, D., Bash, F. N., & Thaddeus, P. 1989, ApJS, 70, 731

Linsky, J. L., Gagné, M., Mytyk, A., McCaughrean, M., & Andersen, M. 2007, ApJ, 654, 347

Marigo, P., Girardi, L., Bressan, A., Groenewegen, M. A. T., Silva, L., & Granato, G. L. 2008, A&A, 482, 883

Megeath, S. T. 1994, in the Structure and Content of Molecular Clouds 25 Years of Molecular Radioastronomy, ed. T. L. Wilson & K. J. Johnston (Heidelberg: Springer) 215

Megeath, S. T., et al. 2004, ApJS, 154, 367

Megeath, S. T., Biller, B., Dame, T. M., Leass, E., Whitaker, R. S., & Wilson, T. L. 2002, in ASP Conf. Ser., 267, Hot Star Workshop III: The Earliest Stages of Massive Star Birth, ed. P. A. Crowther (San Francisco: ASP), 257

Megeath, S. T., Biller, B., Dame, T. M., Leass, E., Whitaker, R. S., & Wilson, T. L. 2003, Rev. Mex. Astron. Astrofis. 15, 151

Megeath, S. T., & Wilson, T. L. 1997, AJ, 114, 1106

Meyer, M., Calvet, N., & Hillenbrand, L. A. 1997, AJ, 114, 288

Meynet, G., Maeder, A., Schaller, G., Schaerer, D., & Charbonnel, C. 1994, A&AS, 103, 97

Muench, A. A., Lada, C. J., Luhman, K. L., Muzerolle, J., & Young, E. 2007, AJ, 134, 411

Ogura, K. 2006, Bull. Astron. Soc. India, 34, 111

Ogura, K., Sugitani, K., & Pickles, A. 2002, AJ, 123, 2597

Ojha, D. K., et. al. 2004a, ApJ, 608, 797

Ojha, D. K., et. al. 2004b, ApJ, 616, 1041

Oye, M. S., Watson, A. M., Kern, K., & Walth, G. L. 2005, AJ, 129, 393

Pandey, A. K., Nilakshi, Ogura, K., Sagar, R., & Tarusawa, K. 2001, A&A, 374, 504

Pandey, A. K., Ogura, K., & Sekiguchi K. 2000, PASJ, 52, 847

Pandey, A. K., Sharma, S., & Ogura, K. 2006, MNRAS, 373, 255

Pandey, A. K., Sharma, S., Ogura, K., Ojha, D. K., Chen, W. P., Bhatt, B. C., & Ghosh, S. K. 2008, MNRAS, 383, 1241

Pandey, A. K., Upadhyay, K., Nakada, Y., & Ogura, K. 2003, A&A, 397, 191

Pandey, A. K., Upadhyay, K., Ogura, K., Sagar, R., Mohan, V., Mito, H., Bhatt, H. C., & Bhatt, B. C. 2005, MNRAS, 358, 1290

Robin, A. C., Reyle, C., Derriere, S., & Picaud, S. 2003, A&A, 409, 523

Robitaille, T. P., Whitney, B. A., Indebetouw, R., Wood, K., & Denzmore, P. 2006, ApJS, 167, 256

Ryter, C. E. 1996, Ap&SS, 236, 285

Salpeter, E. E. 1955, ApJ 121, 161

Sanchawala, K., et al. 2007, ApJ, 667, 963

Sato, M., et al. 2007, PASJ, 59, 743

Sato, M., et al. 2008, PASJ, 60, 975

Schmidt-Kaler, Th. 1982, in Landolt-Börnstein: Numerical Data and Functional Relationship in Science and Technology, Vol. Vi/2b, ed. K. Schaifers & H. H. Voigt (Berlin: Springer), 19

Sharma, S., Pandey, A. K., Ojha, D. K., Chen, W. P., Ghosh, S. K., Bhatt, B. C., Maheswar, G., & Sagar, R. 2007, MNRAS, 380, 1141

Sicilia-Aguilar, A., Hartmann, L. W., Briceño, C., Muzerolle, J., & Calvet, N. 2004, AJ, 128, 805

Sicilia-Aguilar, A., Hartmann, L. W., Furesz, G., Henning, Th., Dullemond, C., & Brandner, W. 2006, AJ, 132, 2135

Sicilia-Aguilar, A., Henning, T., Juhasz, A., Bouwman, J., Hartmann, L., & Watson, D. 2009, AIP Conf. Ser., 1094, 23

Siess, L., Dufour, E., & Forestini, M. 2000, A&A, 358, 593

Stetson, P. B. 1987, PASP, 99, 191

Stetson, P. B. 1992, in ASP Conf. Ser., 25, Astronomical Data Analysis Software and System I. Astron. Soc. Pac., ed. D. M. Warrall et al. (San Francisco: ASP), 297

Tapia, M., Costero, R., Echevarria, J., & Roth, M. 1991, MNRAS, 253, 649

Tsuboi, Y., Koyama, K., Hamaguchi, K., Tatematsu, K., Sekimoto, Y., Bally, J., & Reipurth, Bo. 2001, ApJ, 554, 734

Walborn, N. R. 1973, AJ, 78, 1067

Walborn, N. R., Maíz-Apellániz, J., & Barba, R. H. 2002, AJ, 124, 1601

Wegner, W. 1993, Acta Astron., 43, 209

Whitney, B. A., Wood, K., Bjorkman, J. E., & Cohen, M. 2003, ApJ, 598, 1079

Winkler, H. 1997, MNRAS, 287, 481